ORIGINAL ARTICLE

The dynamics of the El Niño–Southern Oscillation diversity in the recharge oscillator framework

Priyamvada Priya[1,2] · Dietmar Dommenget[1,2] · Shayne McGregor[1,2]

Abstract

This study investigates the observed El Niño-Southern Oscillation (ENSO) dynamics for the eastern Pacific (***EP***) and central Pacific (***CP***) events in reference to the canonical ENSO (***T***). We use the recharge oscillator (ReOsc) model concept to describe the ENSO phase space and polar coordinate statistics, based on the interaction of sea surface temperature (***T***) and thermocline depth (***h***), for the different types of ENSO events. We further look at some important statistical characteristics, such as power spectrum and cross-correlation as essential parameters for understanding the dynamics of ENSO. The results show that the dynamics of the ***EP*** and ***CP*** events are very different from each other and from the canonical ENSO events. The canonical ENSO (***T***) events fit closest to the idealised ReOsc model and has the most clearly oscillating ENSO phase space, suggesting it is the most predictable ENSO index. The ***EP*** phase space evolution is similar to the canonical ENSO, but the phase transitions are less clear, suggesting less of an oscillatory nature and that the index is more focussed on extreme El Niño and discharge states. The ***CP*** phase space, in turn, does not have a clear propagation through all phases and are strongly skewed towards the La Niña state. The interaction between ***CP*** and ***h*** are much weaker, making the mode less predictable. Wind forced shallow water model simulations show that the ***CP*** winds spatial pattern do not force significant ***h*** tendencies, strongly reducing the delayed negative feedback, which is essential for the ENSO cycle.

1 Introduction

El Niño-Southern Oscillation (ENSO) is a naturally recurring pattern that originates through the interplay between atmosphere and ocean in the tropical Pacific Ocean, and it has a significant impact on global climate and society (Philander 1989; Webster et al. 1998; Tudhope et al. 2001; McPhaden et al. 2006; Wolter and Timlin 2011; Yu and Giese 2013; Capotondi et al. 2015; Yeh et al. 2018; Timmermann et al. 2018; Capotondi and Ricciardulli 2021). One of the key features of ENSO is the fluctuations in the SST in the central/eastern equatorial Pacific Ocean. The SST in this region can warm or cool by up to 3 °C during an event, occurring roughly every 2–7 years, causing shifts in the ocean's thermal structure as well as variations in atmospheric circulation and convective activity (Wang and Picaut 2004; Okumura and Deser 2010; Bellenger et al. 2014; Okumura 2019).

ENSO is comprised of two phases: warm phase (El Niño) with a positive SST anomaly (SSTA) and cold phase (La Niña) with a negative SSTA in the eastern and central equatorial Pacific Ocean (Chen and Li 2021). El Niño and La Niña events display general differences in their amplitude, pattern, spatial pattern, temporal evolution, and dynamical mechanisms (Dommenget et al. 2013; Capotondi et al. 2015; Okumura 2019; Capotondi et al. 2020).

Many recent studies have focussed on categorizing the ENSO continuum into events of two distinct types based on SST anomaly differences in the central/eastern equatorial tropical pacific. For instance, an El Niño event can either be classified as eastern pacific (***EP***) or central pacific (***CP***) type, where the different event types respectively have positive SSTA centred over the eastern and

✉ Priyamvada Priya
   priyamvada.priya@monash.edu

1   School of Earth, Atmosphere and Environment, Monash University, Melbourne, VIC, Australia

2   ARC Centre of Excellence for Climate Extremes, Melbourne, VIC, Australia

central equatorial pacific (Kao and Yu 2009; Jeong et al. 2017; Kirtman 2019; Capotondi and Ricciardulli 2021). Therefore, it is essential to investigate these two distinct types of ENSO events in order to have a better understanding of ENSO diversity and its dynamics.

According to a previous study by Kao and Yu (2009), the *EP* events are more influenced by the thermocline and surface wind variation, whereas the *CP* events are more influenced by the atmospheric forcing and less by thermocline variability. In addition to this, many studies argued that the *EP* event is driven by the mean vertical advection of anomalous vertical temperature gradient, referred to as thermocline feedback, whereas the *CP* event is controlled by zonal advection of mean temperature gradient, known as zonal advective feedback (Xie and Jin 2018; Kirtman 2019; Okumura 2019).

Additionally, ENSO phase asymmetries exist in the equatorial tropical Pacific Ocean with stronger El Niño (positive events) and weaker La Niña (negative events), which may be caused by the non-linear wind response to SST (An and Jin 2004; Ohba and Ueda 2009; Frauen and Dommenget 2010). These asymmetries in the amplitude of ENSO's warm and cold events (Choi et al. 2013) imply that ENSO has non-linearities in its spatial and temporal pattern (Takahashi et al. 2011; Dommenget et al. 2013). As a result, it is essential to explore these discrepancies in the pattern of the events, and asymmetries in the El Niño and La Niña for the *EP* and *CP* modes, to further understand the dynamics of ENSO.

The aim of this study is to investigate the dynamics of ENSO diversity. Namely we will focus on analysing the differences in the dynamics of *EP* and *CP* events. The starting point of our analysis is the recharge oscillator (ReOsc) model (Jin 1997; Burgers et al. 2005). It describes the variability of ENSO as an interaction between the tendencies of sea surface temperature anomaly in the eastern equatorial Pacific (*T*) and equatorial mean thermocline depth anomaly (*h*). This model has previously been used in several studies to describe the dynamics of ENSO (Jin 1997; Burgers et al. 2005; Frauen and Dommenget 2010; Yu et al. 2016; Vijayeta and Dommenget 2018; Wengel et al. 2018; Dommenget and Vijayeta 2019; Crespo et al. 2022; Dommenget and Al-Ansari 2012).

The ReOsc model assumes one fixed SST pattern, with the SST index from the eastern equatorial pacific (*T*) and describes the dynamics of this pattern as a damped oscillation with oceanic thermocline depth (*h*). This approach can be used to define an ENSO phase space of *T* and *h* (Meinen and McPhaden 2000; Kessler 2002). Recent studies by Dommenget and Al-Ansari (2012) and Dommenget et al. (2023) analysed the dynamical characteristics of the ENSO phase space in detail, defining growth rates, phase speeds and ENSO strength as function of the ENSO phase.

In this study we will define ReOsc models based on the *CP* and *EP* indices (Takahashi et al. 2011; Dommenget et al. 2013) and compare against the original canonical ReOsc model to understand the differences in the dynamics of these events. We will illustrate how the ENSO phase spaces of *CP* and *EP* differ from each other and from the canonical ENSO. In particular, we aim to determine if it is possible to describe both events as a dynamical cycle, similar to the canonical ENSO, and if not, what are the reasons for this.

The rest of this study is organised as follows: data and methods section, shortly describes the datasets used, the ReOsc model and the phase space analysis methods used. This is followed by the first results Sect. 3, in which we present the ENSO phase space for the different ENSO indices. In the Sect. 4 we fit linear ReOsc models to the data to understand how growth rates, coupling and forcing terms differ between different ENSO types. The final results section focusses on the analysis of the thermocline and wind stress forcings. We conclude the study with a summary and discussion section.

2 Data and methods

2.1 Observations

We use five different data sets for SST and the thermocline depth estimates: the Hadley Centre global sea Ice coverage and SST (HadISST) (Rayner et al. 2003), UK Met Office Hadley Centre 'EN' series observations datasets, version 4 (EN4) (Good et al. 2013) respectively from 1980 to 2021, the reanalysis datasets from Simple Ocean Data Assimilation version 3 (SODA3) (Carton and Giese 2008) (1980–2017), Ocean Reanalysis System 5 (ORAS5) (1980–2018) (Zuo et al. 2019), and CMCC Historical Ocean Reanalysis system: CHOR AS and CHOR RL (1980–2010) (Yang et al. 2017). We concatenate these 5 different datasets for SST and thermocline depth estimates to one dataset for the period 1980–2021. As such, most years are repeated five times, providing a more accurate estimation of the observed variability. Anomalies are defined by removing the mean seasonal cycle (calculated over the full period) from the data. For the estimation of uncertainties (shaded area in the Figures), we assume a decorrelation time of 8 month and assume that the five data sets are essentially representing the same data. Thus, we estimated the number of independent samples in the 40yrs time series to be 60. For *EP/CP* composites plots, 13 independent samples are taken into consideration (there are total 13 events for *EP* and *CP* each).

The equatorial Pacific Ocean thermocline depth (*h*) is estimated based on the maximum gradient in the temperature profile (Z_{mxg}) following the approach of Dommenget et al. (2023). They illustrated that Z_{mxg} is a better proxy

of h for the analysis of the ENSO dynamics in the ReOsc model framework than the widely used depth of the 20 °C isotherm (Z_{20}). Specifically, the h index is calculated by averaging Z_{mxg} over the equatorial pacific region (5°S–5°N, 130°E–80°W).

The 10-m surface zonal and meridional wind data sets are taken from the European Centre for Medium-Range Weather Forecasts (ECMWF-ERA5) reanalysis (1980–2021) (Hersbach et al. 2020). The zonal wind stress data sets are taken from SODA3 (Carton and Giese 2008) (1980–2017), ORAS5 (1980–2018) (Zuo et al. 2019), and CHOR AS and CHOR RL (1980–2010) (Yang et al. 2017) to analyze the wind stress in relation to ENSO variability.

2.2 The ReOsc model

The ReOsc model is based on two tendency equations as given below (Burgers et al. 2005):

$$\frac{dT(t)}{dt} = a_{11}T(t) + a_{12}h(t) + \xi_1 \tag{1}$$

$$\frac{dh(t)}{dt} = a_{21}T(t) + a_{22}h(t) + \xi_2 \tag{2}$$

It describes the anomalies tendencies of a SST index (T) and a thermocline depth index (h), where a_{11} and a_{22} are the growth rates of T and h, respectively, a_{12} and a_{21} are the coupling factors between T and h, and ξ_1 and ξ_2 are the noise forcing of T and h, respectively.

We base the T index for the ReOsc model on different SST indices: T, CP, and EP index. The NINO3 region (5°S–5°N, 150°W–90°W) is the default T index. The mean equatorial thermocline depth anomaly (h) has been used all three indices (T, CP, and EP). In the analysis sections we will discuss how this may affect the presentation.

2.3 CP and EP event separation

Our definition of CP and EP indices is based on the empirical orthogonal function (EOF) of SSTA over the equatorial pacific region (30°S–30°N, 120°E–70°W), following the approach in previous studies (Takahashi et al. 2011; Dommenget et al. 2013). CP and EP indices have been defined as an orthogonal rotation of the first and second principal components (PC 1 and 2) as indicated below:

$$EP = (PC1 + PC2)/\sqrt{2} \tag{3}$$

$$CP = (PC1 - PC2)/\sqrt{2} \tag{4}$$

The CP and EP SSTA patterns, which are calculated by linear regression of SSTA with the respective indices, are

shown in Fig. 1a, b. Similar patterns have been also observed in previous studies (Takahashi et al. 2011; Dommenget et al. 2013). The SSTA pattern of the EP mode peaks toward the eastern equatorial pacific and is confined near the equator. In contrast, the CP mode peaks toward the central equatorial pacific and has a broader meridional extent.

The probability density function (pdf) of the CP and EP indices are shown in Fig. 1c, d. The EP index has a tendency towards extreme positive events (El Niño) with a positive skewness, $\gamma_1 = 1.5$. In turn, the CP index has a tendency towards extreme negative events (La Niña) with a negative skewness, $\gamma_1 = -0.5$. These statistics are similar to Dommenget et al. (2013).

For both the CP and EP patterns, the overlaying wind stress vectors have significantly greater magnitude over the peak SSTA pattern (Fig. 1a, b). Additionally, the different spatial characteristics of these wind stress vectors emphasises the distinct atmospheric processes that drive these patterns. The wind stress vectors are directed towards the eastern equatorial Pacific for the EP mode, while they are concentrated over the central Pacific Ocean for the CP mode. Furthermore, the wind stress vectors have a pronounced meridional extent in the context of the CP mode, which includes a wider latitudinal range. In contrast, the vectors for the EP mode have a much narrower latitudinal distribution, aligning more closely with the equatorial region.

Later in this manuscript we also focus some of our analysis on strong ENSO events. Thus, here we utilise a one standard deviation threshold for the 6 months running mean EP/CP indices to select strong EP/CP events with the month of the peak value set as the reference event time, see Fig. 2a, b.

There are 13 events considered for the EP and CP modes. In the EP mode, 7 out of 13 events are positive, while 6 are negative, whereas, in the CP mode, 6 out of 13 events are positive, while 7 are negative. Additionally, it is seen that the EP modes have stronger positive events as compared to the CP modes, whereas the CP modes have stronger negative events than the EP modes.

2.4 Phase space transformation

For the analysis of the ENSO phase space and the ReOsc model fit we normalize T and h by dividing by their standard deviations, defining T_n and h_n, respectively. The ReOsc model parameters are estimated by a multivariate linear regression on the monthly mean tendencies of T and h with respect to their monthly mean T_n and h_n (Burgers et al. 2005; Jansen et al. 2009; Dommenget and Al-Ansari 2012). The resulting model parameters for the three different ReOsc model fits are shown in Table 1. The 95% confidence interval of the parameters in Table 1 are estimated by the multivariate linear regression function.
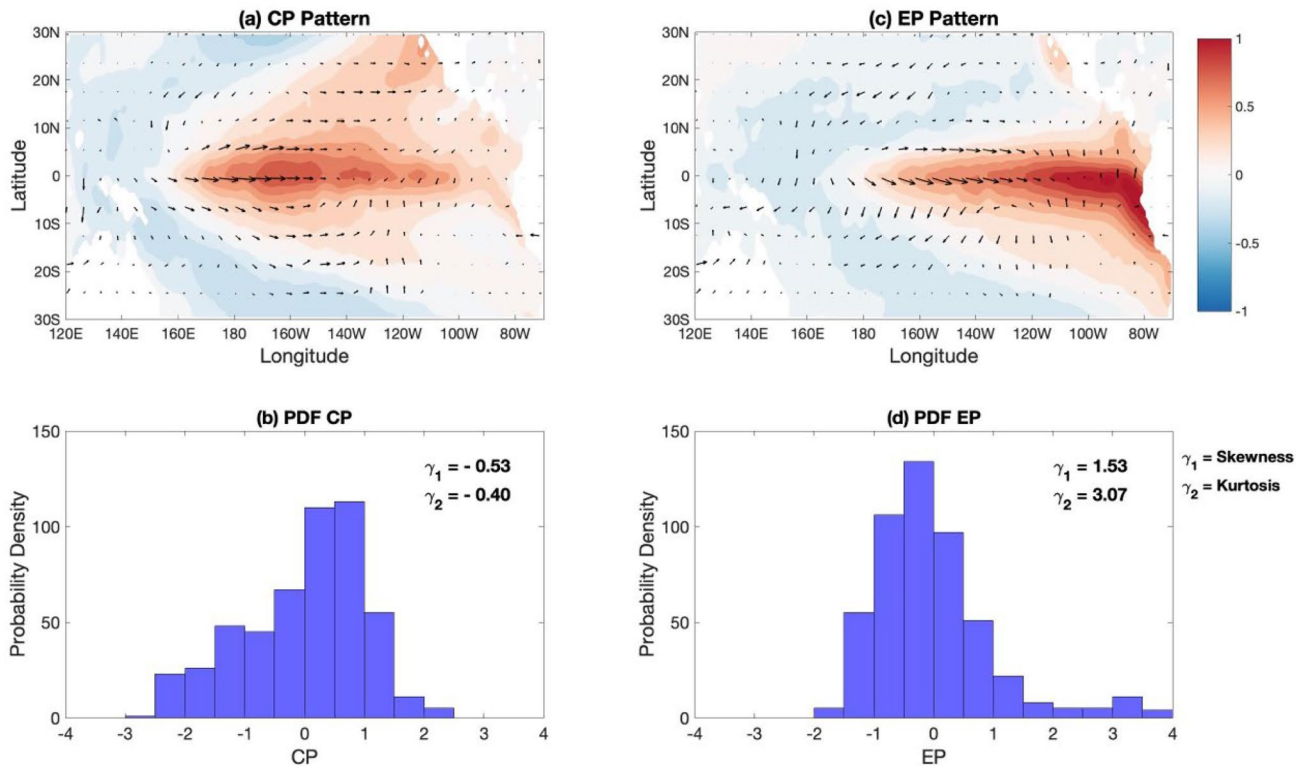
Fig. 1 a *CP* pattern with SST anomalies (shading) by using EOFs and wind stress patterns (vectors) by using linear regression on *CP*, and **b** *EP* pattern with SST anomalies (shading) by using EOFs and wind stress patterns (vectors) by using linear regression on *EP* for the period 1980–2021. The associated probability density distribution functions for **c** *CP*, and **d** *EP* with skewness (γ1) and kurtosis (γ2) parameters

We integrate each of the three models with random white noise forcings for 10^4 years to estimate the statistics of T_n and h_n for each model. We further define an idealised ReOsc model with symmetrical parameters following Dommenget and Al-Ansari [2022]:

$$a_{11} = a_{22} = -0.048\,\text{mon}^{-1} \text{and } a_{12} = -a_{21} = 0.16\,\text{mon}^{-1} \quad (5)$$

This model is also integrated 10^4 years to estimate the statistics of T_n and h_n. We further use this idealised ReOsc model to define confidence intervals for same statistics discussed in this study.

We are following the Dommenget and Al-Ansari (2012) concept for the ENSO phase space analysis. The ENSO phase space is depicted, with T_n along the x axis and h_n along the y axis. A conversion from the cartesian coordinate system to the polar coordinate system has been made, which has a phase angle, φ = 0° in the y-direction (**h**), and 90° in the x-direction (**T**), rotating in a clockwise direction. The ENSO system anomaly, *S* is depicted by a vector, which is represented by two cartesian coordinates T_n and h_n. When it is presented in the polar coordinate system, the magnitude of *S* remains constant for a constant radius

and is not impacted by the phase angle, φ. Thus, the ENSO system is described by the magnitude of *S* and the phase angle φ.

In this polar coordinate system, the ENSO system tendencies are separated into radial and tangential components. The phase-dependent growth rate is calculated by dividing the radial component of the tendencies by the magnitude of *S*, where negative values indicate tendencies towards the origin and positive values indicate tendencies away from the origin. The phase transition speed is calculated by dividing the tangential component of the tendencies by the magnitude of *S*, and it represents the system's tendency to rotate about the origin. Positive values signify a clockwise rotation, while negative values represent an anti-clockwise rotation. Smaller absolute values indicate a slower transition in the ENSO cycle. The mean period of completing one full cycle is calculated by integrating the phase speed from 0° to 360°.

2.5 Simple ocean model experiments

We further use a shallow water model (SWM) to estimate the relation between wind stress forcing and thermocline depth for which **h** is a proxy. The SWM is a linear 1.5-layer
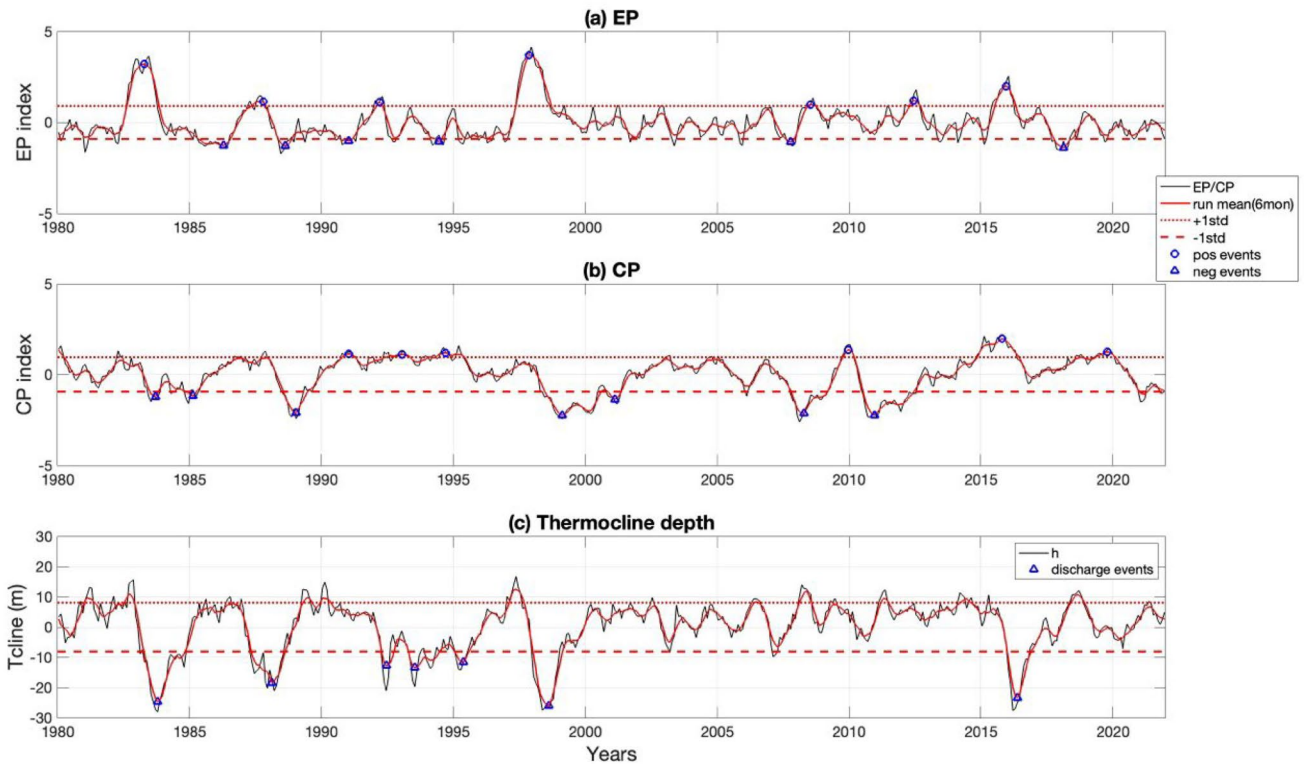
Fig. 2 Time series for **a** *EP* index (black), and selected *EP* events, and **b** *CP* index (black) and selected *CP* events, **c** thermocline depth (black) with selected discharge events (blue triangle) for the period 1980–2021. Running mean (6 months) (solid red line), positive stand- ard deviation (dotted red line), negative standard deviation (dashed red line), selected positive events (blue circle) and negative events (blue triangle). Positive and negative standard deviation threshold are calculated from the 6 months running mean

anomaly model of the sub-tropical to tropical global ocean with a 1° horizontal resolution. The active upper layer (mean depth of H = 300 m) is driven by wind stresses and is separated from the lower motionless, infinitely deep layer by a sharp tropical pycnocline, which approximates the thermocline in the tropical Pacific region (Rebert et al. 1985). Details of the model can be found in McGregor et al. (2007) and Neske and McGregor (2018; their Text S1).

Here we run three different wind forced simulations with the SWM. The first SWM simulation, which we refer to as a control simulation, is forced with monthly average anomalous ERA-Interim wind stresses over the period 1980–2015 (Dee and Uppala 2009), inclusive. The daily wind stresses are calculated using the quadratic stress law:

$$(\tau_x, \tau_y) = \rho_a C_d (U_{10}, V_{10}) \sqrt{(U_{10})^2 + (V_{10})^2} \qquad (6)$$

with τ_x, τ_y are zonal are meridional wind stress, $\rho_a = 1.2$ kg.m^{-3} being the air density, $C_d = 1.5*10^{-3}$ being a dimensionless drag coefficient and U_{10} and V_{10} being the daily average zonal and meridional winds at 10 m height. This simulation is utilised to provide some context for the thermocline depth changes of the following two experiments, which seek to understand the thermocline depth

response to *CP* and *EP* induced anomalous wind stresses. The first SWM experiment is forced with zonal and meridional wind stresses that are linearly related to the *CP* index (Fig. 1a), where the temporal evolution of the wind stress forcing follows the *CP* index. Our second experiment follows a similar protocol, however, here the *EP* pattern and index are utilised (Fig. 1b). Note, SWM thermocline depth is calculated by the average of the model pycnocline depth over the equatorial Pacific region (5°S–5°N, 130°E–80°W).

3 Observed phase space

We start the analysis with looking at the differences in the ENSO phase spaces between *CP* and *EP*, as well as how they differ from the canonical ENSO (*T*). Figure 3 shows the observed phase space for *T*, *CP* and *EP*. All three presentations of ENSO show distinct features in the phase space and it is clear that the structure of the *CP* phase space is quite different from that of the *EP* and *T* phase space. For the analysis of the *T*, *CP*, and *EP* indices, *h* index which is the Z_{mxg} over the equatorial Pacific region is being used. We will start the discussion with the phase space of *T*, as it provides a reference for the *CP* and *EP* dynamics. Since the
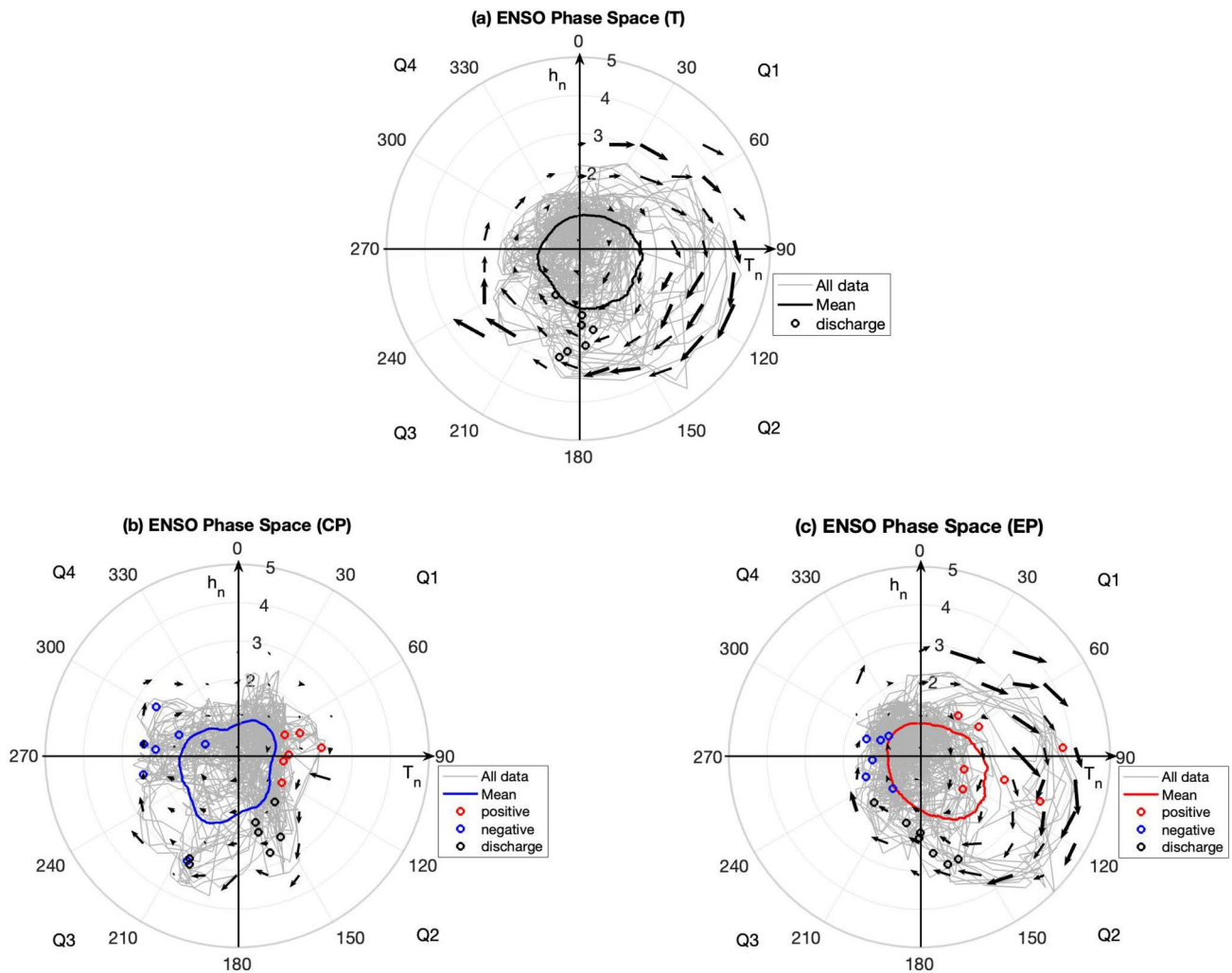
Fig. 3 Statistics of the observed ENSO phase space for **a** *T* with all data (grey) and mean (black), **b** *CP* with all data (grey) and mean (blue), and **c** *EP* with all data (grey) and mean (red). Red circles are the positive, and blue circles are the negative events of *EP* and *CP*. Black circles are the discharge events. Black arrows represent the tendency vectors of mean tendencies of T_n and h_n within a range of ± 0.4 of the reference point in phase space (starting point of the vector). A unit-length vector represents a tendency of 1 mon^{-1}, with the scale of the vector proportional to the magnitude of the tendencies. The tendency vectors are only displayed when $S < 3.5$ and where actual data are available

results for the phase space of *T* are very similar to those discussed in Dommenget et al. (2023), they will only be briefly discussed as a more comprehensive discussion is given in Dommenget et al. (2023).

The phase space of *T* shows similarities to an idealised damped oscillator with noise forcing and a clear clockwise propagation through all phases. However, the variability is skewed towards stronger positive *T* values (El Niño) and more negative *h* values (discharge). The vectors illustrating the means tendencies of T_n and h_n are cyclically rotating in a clockwise orientation. The phase propagations (clockwise tendencies) are more pronounced in quarter Q2 (transition from El Niño to discharge) and less pronounced in Q4 (transition from La Niña to recharge).

The phase space of *EP* is similar to that of *T*, but it does have some clear deviations from it. First, the *EP* phase space is more pronounced along the diagonal of Q2 to Q4 and less pronounced along the diagonal of Q1 to Q3. This suggests an in-phase negative correlation between *EP* and *h*. Further, the phase propagation in the *EP* phase space is clearer in Q1 (from recharge to El Niño) and less clear in Q3 and Q4 (from discharge to La Niña to recharge) than for the phase space of *T*. In summary, the *EP* phase space fits less to the idealised ReOsc model idea than the phase space of *T*.

The *CP* phase space is quite different from the *T* and *EP* phase space and is also quite different from the idealised ReOsc model idea. It is clearly skewed towards negative *CP* values (La Niña) consistent with previous studies (e.g.,

Takahashi et al. 2011, Dommenget et al. 2013). A phase propagation is much weaker and less clear in the *CP* phase space than in the *T* and *EP* phase space, but is still mostly, weakly clockwise.

The main features in the phase space of *T*, *CP* and *EP* are quantified by some mean statistics in Fig. 4. Here we focus on the mean *S*, the probability of *S* > 2, the growth rate and the phase speed as function of the phase (see methods section for details). We compare each of these statistics in the *CP* and *EP* against the *T* phases space as a reference, and against an idealised ReOsc model. The latter serves as a reference to an entirely symmetric phase space with the same limited, 40yrs time series. Thus, it provides a confidence interval for the null hypothesis that there are no phase-depending structures in the phase space.

The phase space statistics of *EP* are overall quite similar to that of *T*, but we can see some deviations. Both, the phase-dependence of the mean *S* and the probability of *S* > 2 are more pronounced than for the phase space of *T*. They centre even more clearly on the Q1 (El Niño transition to discharge). The growth rate of the *EP* phase space is also similar to that of the phase space of *T*, but it fluctuates more strongly along the different phase, and it is more strongly negative for the phases from 150° to 270° degrees (discharge to La Niña state).

The mean phase speed of *EP* shows the largest deviations from the *T* phase space. It is in general smaller, suggesting a slower ENSO cycle for the *EP* phase space than for the *T* phase space. A smaller mean phase speed, assuming the same spread within the phase speeds (not shown), can also be interpreted as a less clear transition through the ENSO phases. It is in particular smaller in the transition from El Niño to discharge (Q2), but very similar to the *T* phase space in the transition from recharge to El Niño. If we integrate the phase speed over the whole cycle, we find a full cycle period of 53mon for *EP* and 45mon for the *T* phase space.

If we look at how the different statistics combine to the evolution of the *EP* phase space, we can note that in Q3 the slower phase speed and more negative growth rate go along with lower mean *S* and lower probability of *S* > 2. This suggest that the *EP* El Niño event decline faster after the discharge state than the *T* phase space, indicating that the *EP* phase cycle is somewhat collapsing in this phase.

Focussing now on the *CP* phase space, we can note that the statistics now more clearly deviate from the *T* phase space (Fig. 4a–d). The mean *S* and the probability of *S* > 2 are clearly shifted towards the La Niña state, as also pointed out above. The phase-dependence of the growth rate is also quite different from that of *T* phase space (Fig. 4c). For the *T* phase space, the growth rate is positive over a wide range of phases starting in Q4, going through all of Q1 and most of Q2, and then transition into a negative growth rate in Q3. This large-scale phase-dependence of the growth rate is not

present in the *CP* phase space at all. In contrast, it varies more strongly between positive and negative growth rate in Q4 and Q1 and stays close to neutral in Q3. In particular, in Q4 (transition from La Niña to recharge state) it has a phase of very strong negative growth rates, which goes along with a collapse in the probability of *S* > 2 and a decline in mean *S*, suggesting that the *CP* phase space is collapsing in the transition from La Niña to recharge state.

The mean phase speed of *CP* is much smaller than for the *T* phase space in nearly all phases (Fig. 4d). It also shows strong variations, with the slowest phase speed in Q1, and much larger phase speed in Q3 and Q4. However, it is significantly positive in all phases, suggesting that there is clockwise phase transition through all ENSO cycles in the *CP* phase space. The integrated phase speed over the whole cycle gives a full cycle period of 79mon, which is much longer than for the *T* phase space. However, the overall much smaller mean phase speed also suggests that the *CP* cycle is much less clear than for the *T* phase space.

The results of the phase space analysis suggest that the *CP* phase space has a less clear phase transitions than the *EP* or *T* phase space, which indicates that the out-of-phase correlation between *CP* and *h* should be weaker, and the power spectrum of the *CP* index should have a less prominent peak, that should be shifted to longer periods. In Fig. 5 both of these characteristics can be seen in the cross-correlation between *CP* and *h* (Fig. 5a) and in the power spectrum of the *CP* index (Fig. 5b). The out-of-phase cross-correlation between *CP* and *h* is clearly weaker than between *T* and *h*, in particular when *T* leads *h*, which is the transition from large *CP* values (El Niño/La Niña) to large *h* values (discharge/recharge). This suggests that the *CP* index has a weaker SST forcing on the *h* tendencies than the *T* index.

The power spectrum of the *CP* index has no clear interannual peak, unlike the *EP* and *T* index that both peak at periods around 4–5 years, consistent with what we find from the mean phase speed analysis. The *CP* index has more of a red noise (Hasselmann 1976) and decadal time scale characteristics than the *EP* and *T* index.

The *EP* index is much more similar to the *T* index than the *CP* index, but still has some important differences. The out-of-phase cross-correlation between *EP* and *h* is weaker than between *T* and *h*, when *h* leads *EP*, which is the transition from large *h* values (recharge/discharge) to large *EP* values (El Niño/La Niña). There is also a significant cross-correlation between *EP* and *h* at lag zero, which does not exist for the cross-correlation between *T* and *h*. These differences in the cross correlation suggests that SST tendencies in the *EP* index are less forced by *h* than for the *T* index. It also suggests a less oscillatory behaviour than the *T* index, which is quantified in the power spectrum of the *EP* index that has a less pronounced interannual peak than the *T* index (Fig. 5b).
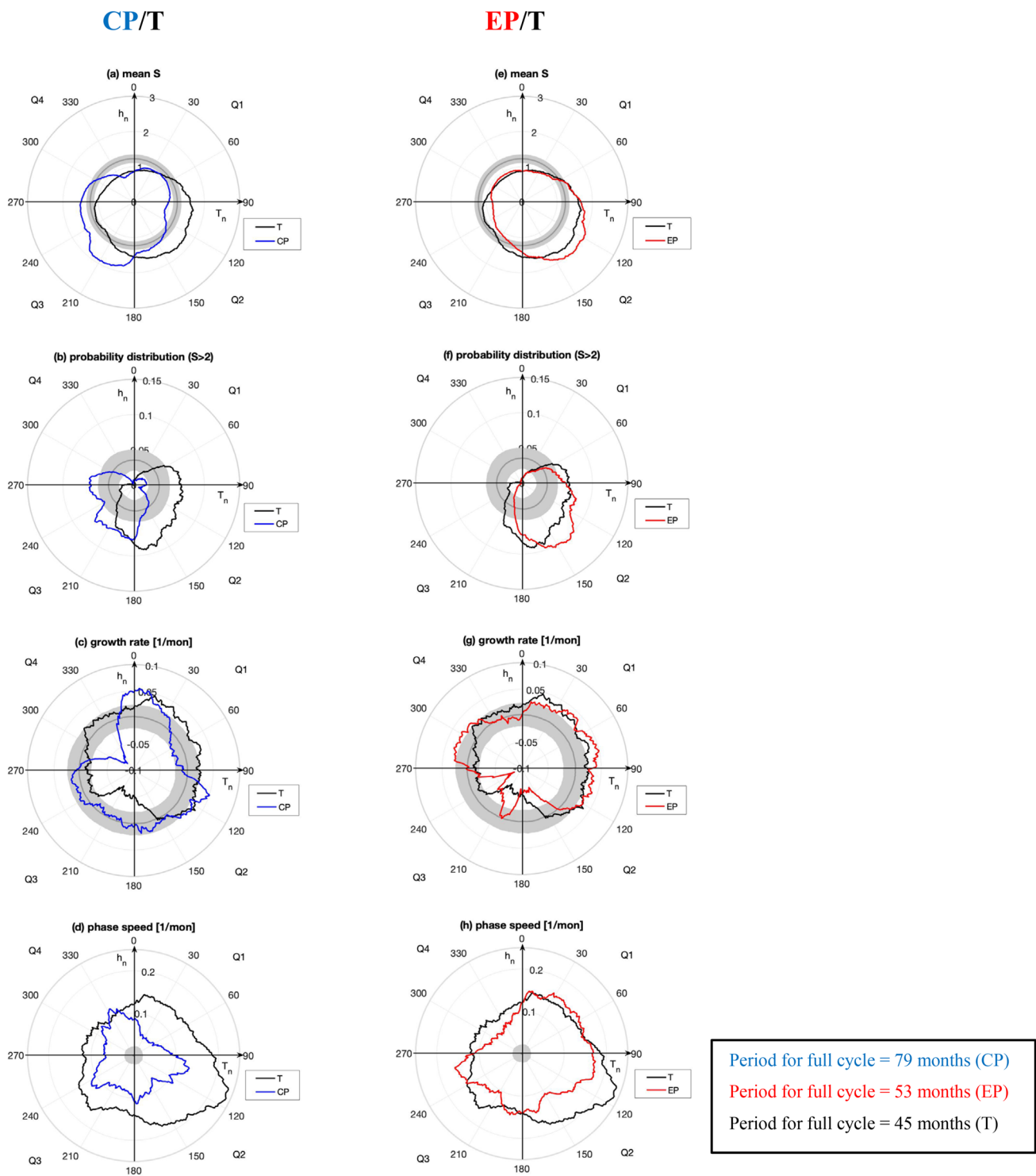
Fig. 4 Statistics of the Observed ENSO phase space with idealised ReOsc model (grey line) and standard error (shaded area) **a** mean **S** for **T** and **CP**, **b** mean probability distribution (**S** > 2) for **T** and **CP**, **c** mean growth rate for **T** and **CP**, **d** mean phase transition speed for **T** and **CP** with uncoupled ReOsc model (grey line) and standard error (shaded area), and **e**, **h** is similar to **a**–**d** but for **T** and **EP**. **T** (black), **CP** (blue), **EP** (red), and **S** is the ENSO system anomaly. In **c** and **g**, the grey circle represents zero growth rates, values inside the circle represent negative, and values outside positive growth rates
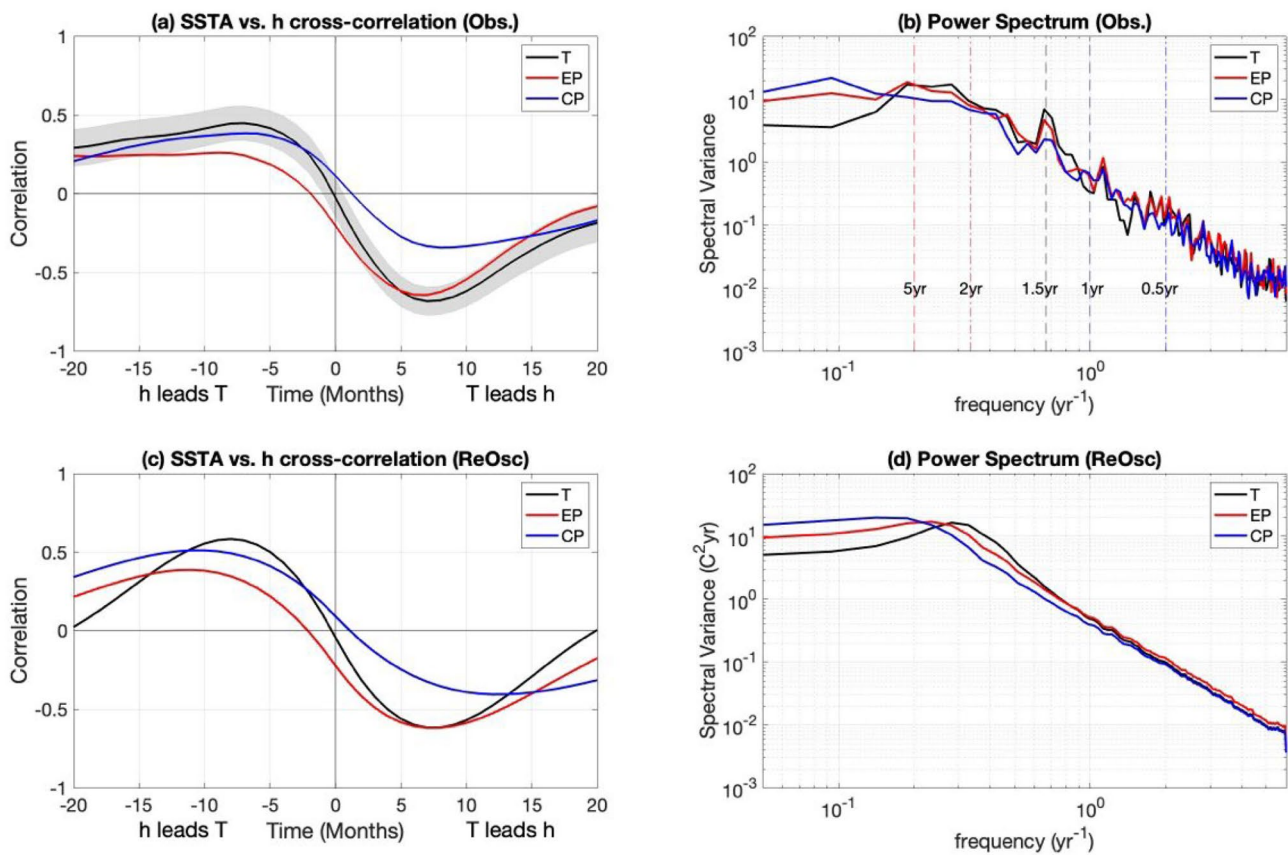
Fig. 5 **a** Cross-Correlation of SSTA vs. h for observed T, EP, and CP with associated standard error (shaded area), and **b** Power spectrum of observed T, EP, and CP. Lower panel is similar as upper panel but for ReOsc model. T (black), CP (blue), and EP (red). Dotted lines in panel **b** are showing the particular years. T is normalised by dividing by the standard deviation of T. EP and CP are normalised as well as it is calculated by the linear combination of PCs associated with the EOFs

4 Fitted ReOsc model

The observed phase space characteristics can be analysed in the ReOsc framework to better understand the underlying dynamics causing these structures. Therefore, the linear ReOsc model parameters (Eqs. 1–2) are fitted to the observed, normalized data for the three different ENSO phase spaces T-h, CP-h and EP-h (see methods section). The resulting parameters for the three different ReOsc models are shown in Table 1.

The integration of these different ReOsc models results into different phase space characteristics that can be compared against the observed phase spaces, see Fig. 6. Here it should be noted, that a linear ReOsc model, by construction, is symmetric for opposite phases, as it is a linear function of T and h (Dommenget and Al-Ansari 2012). The analysis of the ReOsc model parameters and their resulting phase space characteristics gives us some understanding of the underlying dynamics for each of the three ENSO indices.

Starting with the T vs. h phase space we can note that the parameters in the normalised growth rates, coupling

and noise forcings are mostly similar for T and h, and the phase statistics do not have much phase-dependent characteristics. Thus, the T vs. h phase space is similar to an idealised ReOsc model. Some deviations in the probability of $S > 2$ and the phase speed result from the somewhat stronger damping in h than T (compare a_{11} and a_{22} in Table 1). Most of the observed phase-dependent variations cannot be explained by the linear ReOsc model, as has been discussed in Dommenget et al. (2023), suggesting that non-linear processes are likely to causes these asymmetries.

The EP vs. h phase space in the linear ReOsc model fit is similar to that of the T vs. h, but it deviates more strongly from the idealised ReOsc model than T vs. h fit. The ReOsc model fit for EP vs. h has a significantly stronger damping in h and weaker damping in T (compare a_{11} and a_{22} in Table 1), leading to a larger asymmetry in the damping terms. This asymmetry in the growth rates of T (a_{11}) and h (a_{22}) lead to a phase space that is more pronounced along the Q2 and Q4 phases (Fig. 6i, j), which is reminiscent of a negative correlation between EP vs. h (Fig. 5a, c). Further, the coupling of the tendencies of T to h (a_{12}) is significantly
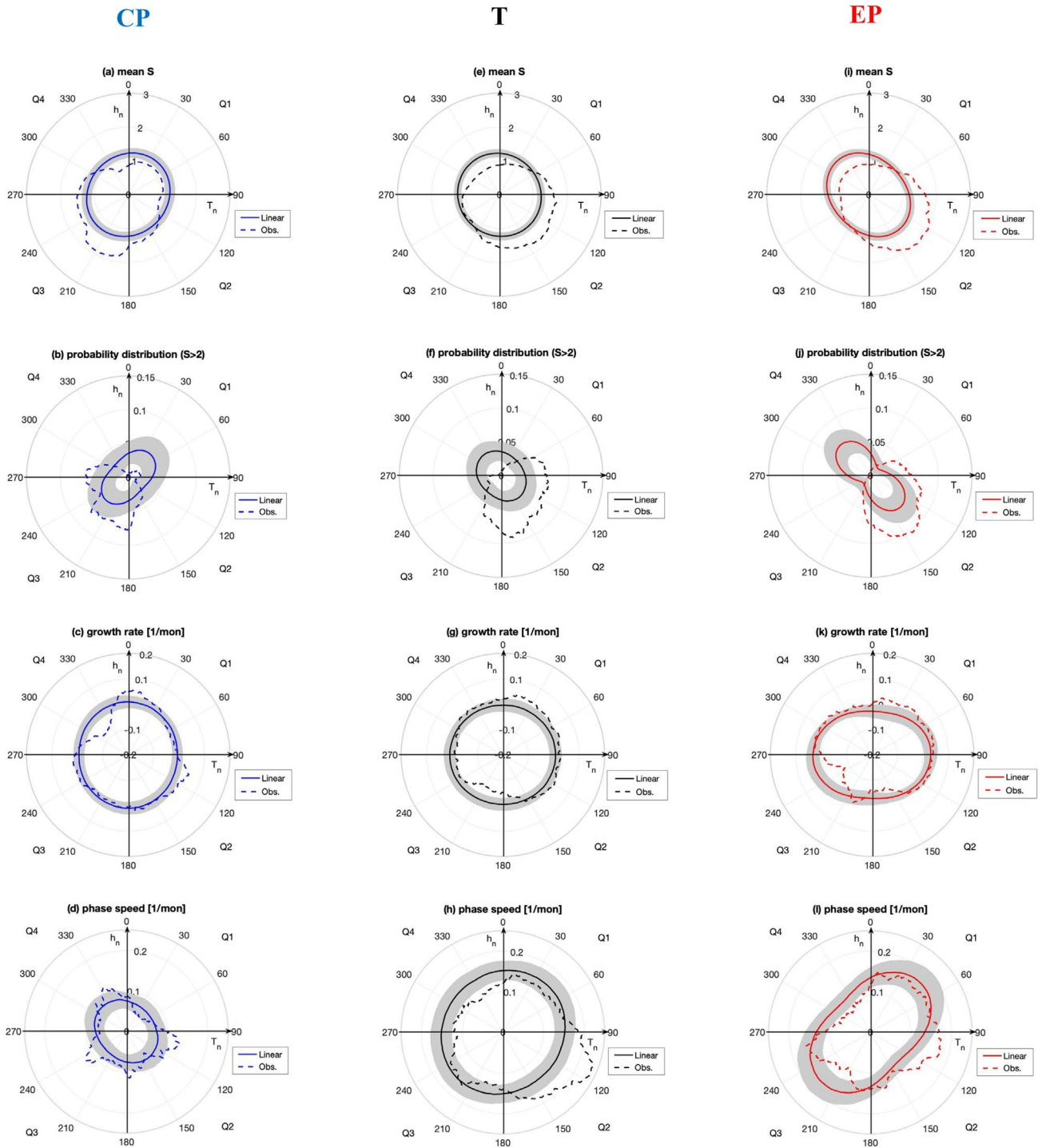
Fig. 6 Statistics of the linear (solid line) and observed (dashed line) ENSO phase space with standard error of linear ReOsc model (shaded area) **a** mean *S* for *CP*, **b** mean probability distribution ($S > 2$) for *CP*, **c** mean growth rate for *CP*, **d** mean phase transition speed for *CP*, and **e–h** similar to **a–d** but for *T*, and **i–l** similar to **a–d** but for *EP*. *T* (black), *CP* (blue), and *EP* (red)

weaker in *EP* vs. *h* fit than in the *T* vs. *h* fit. This reduces the cross-correlation between *EP* and *h,* when *h* leads the *EP* index (Fig. 5c). It further affects the periodicity by shifting it to longer periods and making it less pronounced (less

pronounced peak; Fig. 5c) than for the *T* index, suggesting that the *EP* index is not as clearly oscillating as the *T* index.

The *CP* vs. *h* phase space in the linear ReOsc model fit is quite different from that of *T* and *EP*. The most significant

Table 1 ReOsc model parameters for normalized T and h, CP and h, and EP and h

Normalized ReOsc model parameters

	Tendency parameters	T		CP		EP	
1.	Growth rate (mon^{-1})	$a_{11} = -0.05$	± 0.01	$a_{11} = -0.05$	± 0.01	$a_{11} = -0.04$	± 0.02
		$a_{22} = -0.07$	± 0.01	$a_{22} = -0.06$	± 0.02	$a_{22} = -0.11$	± 0.01
2.	Coupling (mon^{-1})	$a_{12} = 0.15$	± 0.01	$a_{12} = 0.077$	± 0.012	$a_{12} = 0.12$	± 0.01
		$a_{21} = -0.16$	± 0.01	$a_{21} = -0.072$	± 0.015	$a_{21} = -0.16$	± 0.01
3.	Noise Forcing (mon^{-1})	noise-T = 0.29		noise-T = 0.27		noise-T = 0.34	
		noise-h = 0.32		noise-h = 0.36		noise-h = 0.33	

Uncertainty in the parameters for 95% confidence interval (in grey within box)

difference is in the coupling parameters, which are now both only about half as strong as for T vs. h fit (compare a_{12} and a_{21} in Table 1). This leads to a much weaker phase transition speed (compare Fig. 6d vs. h, l) and a much weaker cross-correlation between CP and h (Fig. 5c). This is also reflected in the power spectrum of the CP index, which has a much weaker dominant peak that is shifted to longer periods. The asymmetry in the strength of noise forcing of T (ξ_1) and h (ξ_2) is leading to the asymmetries in the phase space diagrams of the linear ReOsc fit (e.g., enhanced probability distribution for $S > 2$ in quarters Q1 and Q3 or phase speeds in quarters Q2 and Q4; Fig. 6b, d).

For all three different phase spaces we can see clear deviations of the observed characteristics from those of the linear ReOsc model fit. These are mostly asymmetric in the ENSO phases space (different for opposing phases), suggesting that they are representing non-linear dynamics that a linear ReOsc model can by construction not capture. These are most prominent in the extreme events ($S > 2$), but also exist in the other characteristics of the phase space.

In summary, the linear ReOsc model fit can capture much of the differences between the T-h, CP-h and EP-h phase spaces. It clearly illustrates that the coupling between SST and h is different for the CP phase space if compared against EP or T phase spaces. It also illustrated that the T-h phase space is closest to the idealised ReOsc model and the CP-h deviates the most from an idealised ReOsc model.

5 Analysis of the thermocline and wind dynamics of EP and CP events

We now want to take a closer look at the dynamics of the thermocline depth and wind stress in relation to the EP and CP events. We start with analysing the thermocline evolution during ENSO events and then focus on the wind stress.

5.1 Thermocline depth

In the above discussion of the different phase space diagram, we implicitly assumed that the mean equatorial thermocline depth (h) is the correct dynamical variable to describe the phase space evolution for all the three different ENSO indices. However, it is possible that the different ENSO temperature indices are sensitive to the thermocline depth at different zonal regions along the equatorial Pacific. We therefore analyse a Hovmöller diagram of the time evolution of the equatorial thermocline depth for EP and CP events of different signs, see Fig. 7. There are a number of different characteristics that can be noted in the evolution of the equatorial thermocline depth.

First, we can note the zonal structures of the equatorial thermocline depth with the dominant east–west dipole
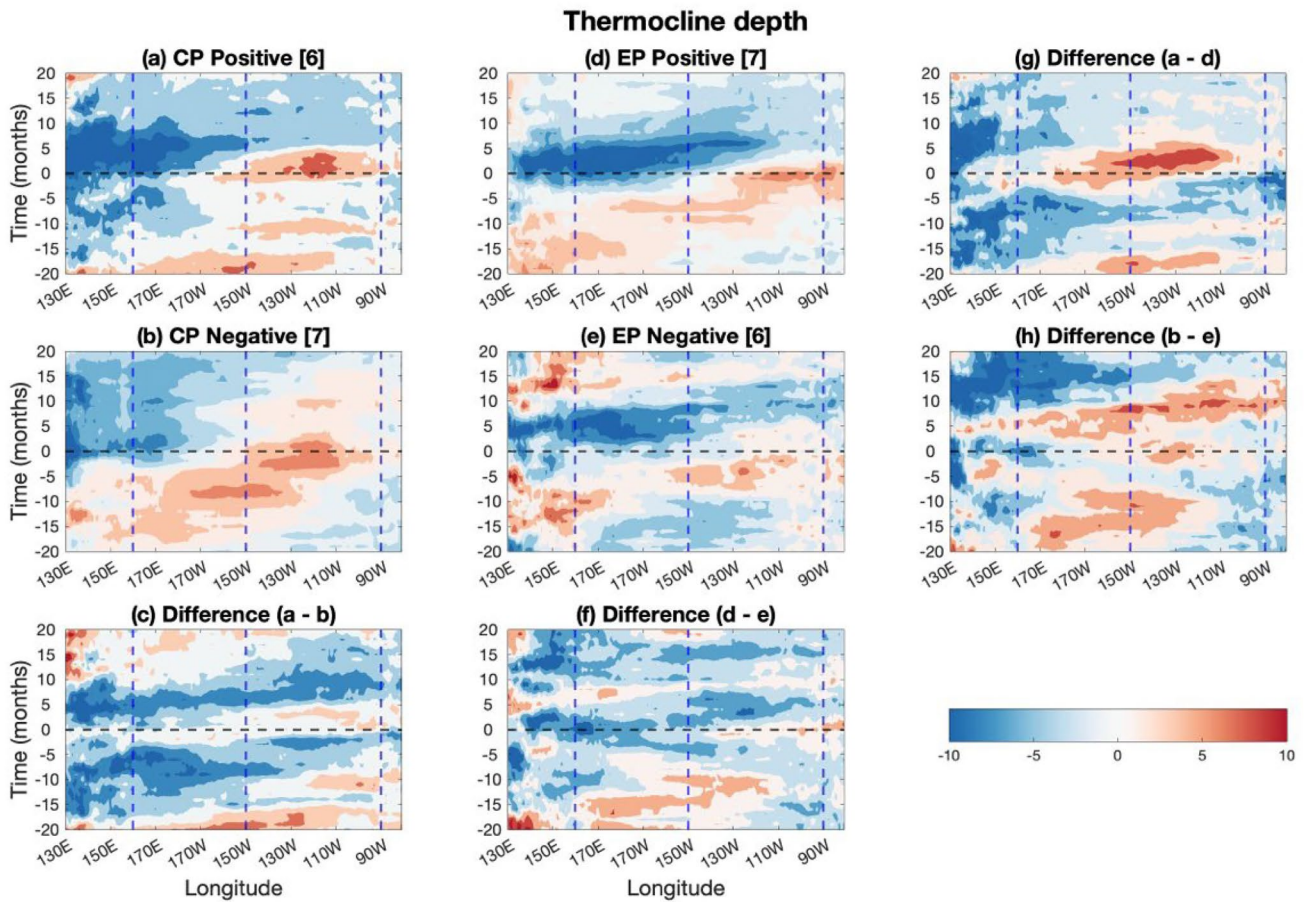
Thermocline depth

Fig. 7 Composite Hovmöller plots of normalised thermocline depth anomaly **a** *CP* positive events [6], **b** *CP* negative events [7], **c** difference of positive and negative events of *CP*, **d** *EP* positive events [7], **e** *EP* negative events [6], **f** difference of positive and negative events of *EP*, **g** difference **a–d**, and **h** difference (**b–e**). Thermocline depth anomaly for *CP* positive have been divided by *CP* index for mean positive events and *EP* positive have been normalised by *EP* index for mean positive events, and similar for negative events. The dashed vertical lines mark the zonal boundaries of the NINO4 (left to centre) and NINO3 (centre to right) regions

(tilting mode) and the less prominent zonal mean mode. The tilting mode is more pronounced during the peak of the events (at lag zero) and the zonal mean mode is more pronounced before and after the events, consistent with the analysis of Meinen and McPhaden [2000].

Secondly, we can note the longitude vs. time relation suggest propagation of equatorial thermocline depth anomalies from the west to the east, which is somewhat faster for the *EP* events than for the *CP* events (e.g., Fig. 7a, b, d, e). This is consistent with the faster phase speeds of the *EP* vs. the *CP* phase spaces (Fig. 4d, h). Further, we can note differences between the different sign of events and the different type of events. The negative *CP* events have a more pronounced thermocline depth evolution than the positive *CP* events (Fig. 7a, b), while the positive *EP* events have a clearer thermocline depth evolution than the negative *EP* events (Fig. 7d, e).

Figure 8 synthetises the structures we have noted in Fig. 7 that are symmetric of negative and positive events. The

faster evolution of the *EP* events that are also more clearly oscillating than the *CP* events are illustrated by the SST evolution in Fig. 8a. Here we can note that the *EP* events are changing signs fast before and after the event peak, whereas the *CP* events evolve more slowly, suggesting that the *CP* events are not clearly oscillating. The mean equatorial thermocline, *h*, evolution shows a very clear decrease, i.e., a discharge about 5mon. after the *EP* events, that is not as strong for the *CP* events (Fig. 8b) (Kug et al. 2009, 2010). This is consistent with the patterns seen in Fig. 7a, b, d, e and the stronger phase transitions speeds of the *EP* phase space for El Niño and La Niña phase in comparison to those of the *CP* phase space (Fig. 4d, h). The tilting mode has a strong in-phase relation to both *EP* and *CP* events (Fig. 8c). This relation is stronger for the *CP* events, which can also be noted by the more pronounced dipole patterns seen in Fig. 7a, b versus those of the *EP* events seen in Fig. 7d, e, which may be partly related to the normalisation by the mean *CP* and *EP* values.
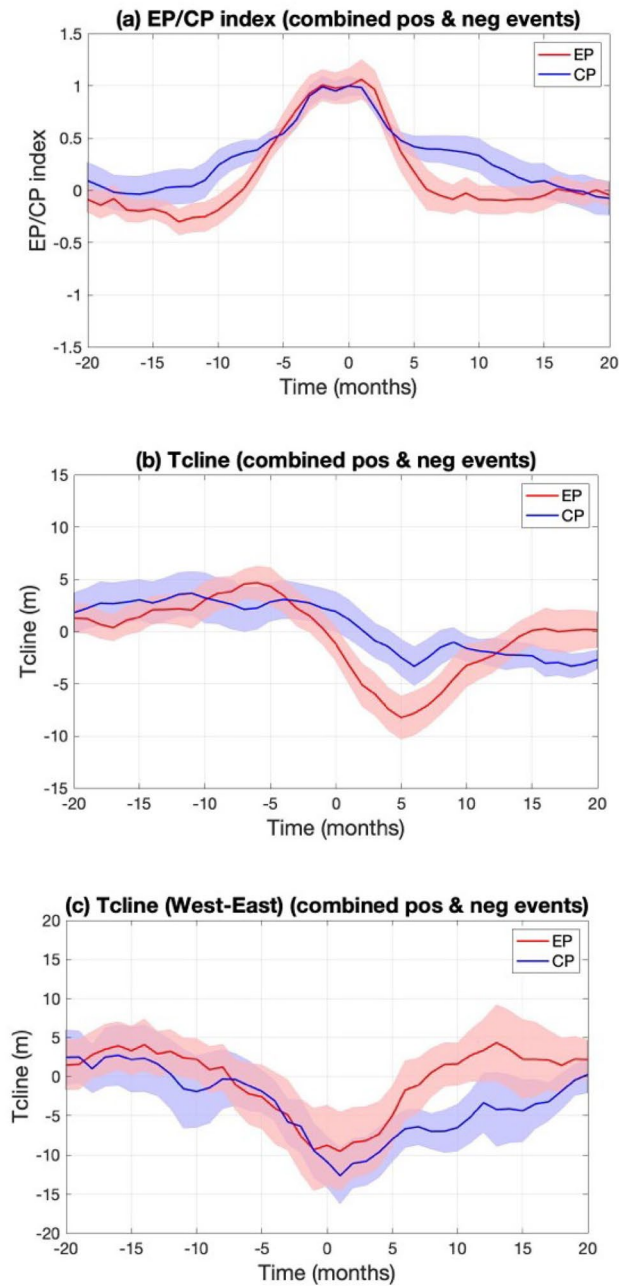
Fig. 8 Time series (solid line) of combined positive and negative events of *EP* (red) and *CP* (blue) events with associated standard error (shaded area) (**a**) *EP/CP* index, and **b** thermocline depth anomaly for equatorial pacific region, **c** thermocline depth anomaly for west box (5°S–5°N, 140°E–180°E) minus east box (5°S–5°N, 150°W–90°W) equatorial pacific region. This west minus east dipole of the thermocline depth anomaly is called tilting mode. *EP/CP* index and thermocline depth anomaly for *EP/CP* have been normalised by *EP/CP* index for mean positive and negative events

We can further analyse the asymmetry between positive and negative events by analysing the cross-correlation between the *EP/CP* indices and the thermocline depth for different event composites, see Fig. 9. We can again notice

that the *EP* events are oscillating more strongly than the *CP* events. In general, we also see that the cross-correlation with the mean thermocline depth (*h*) is more positive at all lags for La Niña (negative) events than for El Niño (positive) events (Fig. 9a, c). This leads to higher cross-correlations when *h* leads the *T* indices for La Niña events, and stronger negative cross-correlations when the *T* indices lead *h* for El Niño events. The tilting mode (west box (5°S–5°N, 140°E–180°E) minus east box (5°S–5°N, 150°W–90°W) of equatorial pacific region) has stronger in-phase correlation for all event types, but has a more negative correlation for *CP* La Niña events than for *EP* La Niña events (Fig. 9b, d).

In summary, we find some significant differences in the SST and thermocline depth interaction for the different SST indices. The *T* and *EP* type of ENSO events have a stronger out-of-phase relation with the equatorial mean thermocline depth (*h*) than the *CP* type, consistent with the results in previous sections. The in-phase relation with the thermocline tilting mode is more pronounced for *CP* negative than for the *EP* negative type. Further, the analysis did not reveal any indication that the *CP* SST tendencies would have a stronger relation with an equatorial thermocline depth index different from the equatorial mean (*h*).

5.2 Wind stress forcing

The zonal wind stress (τ_x) is a key element of the positive Bjerknes feedback (Bjerknes 1969), amplifying ENSO events, it is also the main driver of the delayed negative feedback, by forcing the thermocline depth and zonal current anomalies (Jin and An 1999; Zhu et al. 2015; Izumo et al. 2019) developing after an ENSO events, and the main noise forcing initiating ENSO events.

Figure 10 shows a Hovmöller diagram for the zonal wind stress anomalies along the equatorial Pacific (Izumo et al. 2016) for *CP* and *EP* events. There are a number of differences between *CP* vs. *EP* and between positive vs. negative events. First, we can note that the wind response is primarily in-phase with the SST, thus peaking when the SST is peaking (at lag zero), reflecting that the wind response is primarily positive feedback. It appears to be stronger for positive events than for negative events, for both the *CP* and *EP* events.

Secondly, we can notice that the wind response patterns follow the SST peaks along the equator, with *CP* events further to the west and *EP* events further to the east, which also results into some opposite sign wind response in the NINO3 region for the *CP* events, consistent with previous studies (Ashok et al. 2007; Kao and Yu 2009). Further, we can see some asymmetry of the wind response relative to the timing of the events. For most events the wind forcing is stronger a few months before the events, supporting the build-up of the SST anomalies, and weaker or of reversed sign after
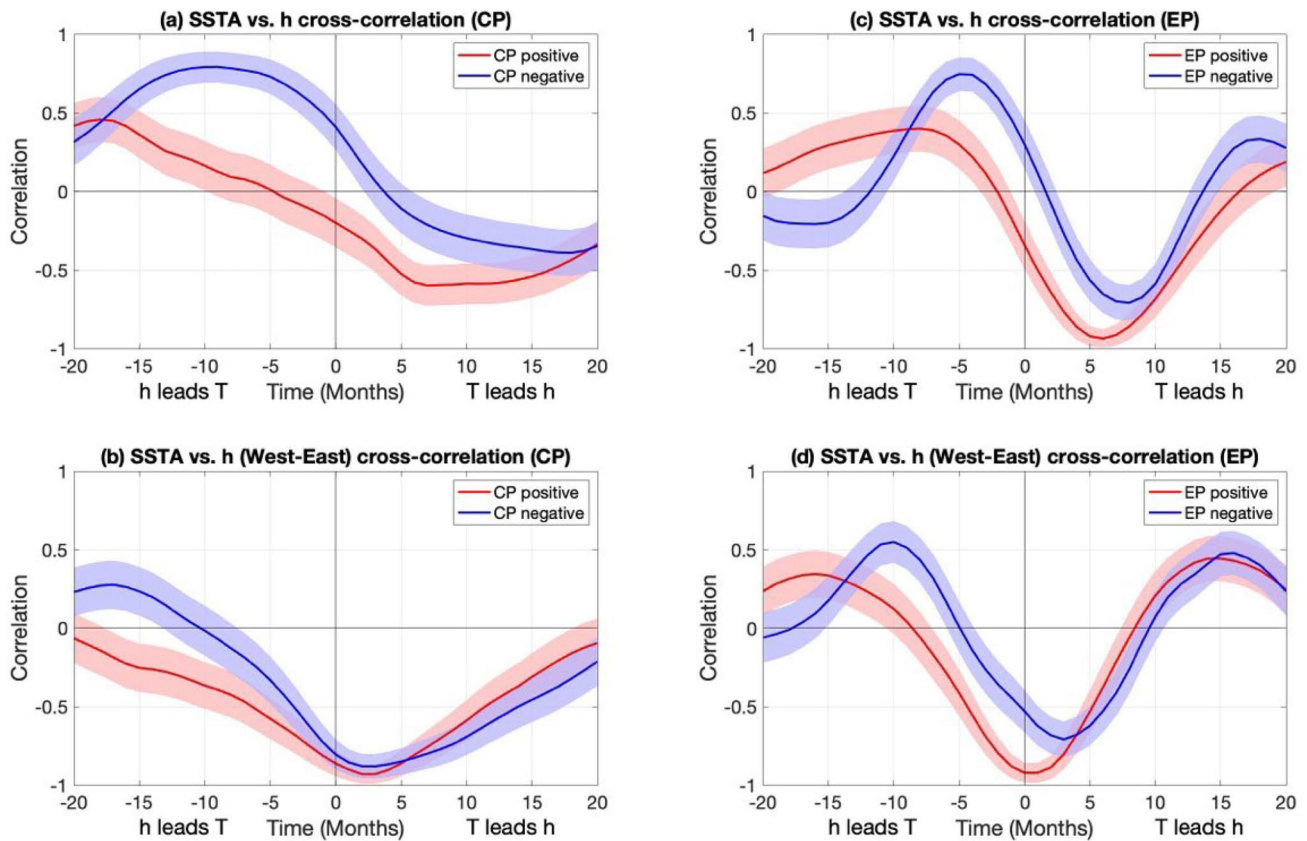
Fig. 9 Cross-Correlation of SSTA for *EP* and *CP* vs. *h* for positive (red) and negative (blue) events with associated standard error (shaded area) for **a** *CP* for equatorial pacific region of *h*, **b** *CP* for west (5°S–5°N, 140°E–180°E) minus east (5°S–5°N, 150°W–90°W) equatorial pacific region of *h*, **c** *EP* for equatorial pacific region of *h*, and **d** *EP* for west minus east equatorial pacific region of *h*

the event. This signature is clearer for the *EP* events, while for the *CP* events there is a long lead wind forcing for the positive events, but not for the negative events (Fig. 10a, b). The latter have a long-lagged response of the winds after the event peak, suggesting the wind support long-lived La Niña events.

Next, we quantify the wind evolution for the different event types in the NINO3 and NINO4 (5°S–5°N, 160°E–150°W) regions, see Fig. 11. First, we notice that the NINO4 wind correlation peaks near lag zero for *CP* events and positive *EP* events. This reflects the positive feedback nature of the wind response to SST anomalies. In addition, there is a tendency for a larger correlation when NINO4 τ_x leads the SST than when SST leads τ_x for positive *EP* events and negative *CP* events at lead time of 1–2mon (Fig. 11a, c), suggesting that the wind forces the SST in these types of events.

Somewhat not consistent with this picture of wind forcing the SST are the negative *EP* events, which have a correlation around zero when τ_x leads SST by 5mon to 7mon and a clearly higher correlation when SST leads τ_x by about 0 to 1mon. Indeed, the largest magnitude in cross-correlation for

these types of events is when τ_x leads SST by about 1mon to 3mon. This long lead cross-correlation may also reflect positive SST anomalies preceding the *EP* events, potentially leading to the negative *EP* events via forcing of the thermocline depth.

The NINO3 wind forcing for the *EP* positive events are slightly higher correlated at short lead times when SST leads τ_x and further, the *EP* negative events do not have a strong correlation over the lead months. The *CP* events show a very different relation to NINO3 wind forcing (Fig. 11b), which have a more prominent out-of-phase relation with the SST, but no strong in-phase correlation (lag zero), in particular for the negative *CP* events. This suggests that the NINO3 region wind are a driver of *CP* La Niña events.

5.3 Wind stress forcing thermocline depth in a shallow water model

The analysis so far suggests that *EP* and *CP* events have quite different relations with *h*. The phase transition speed for *CP* events is significantly smaller than those of the *T* or *EP* index, which could be related to the fact the *CP* pattern
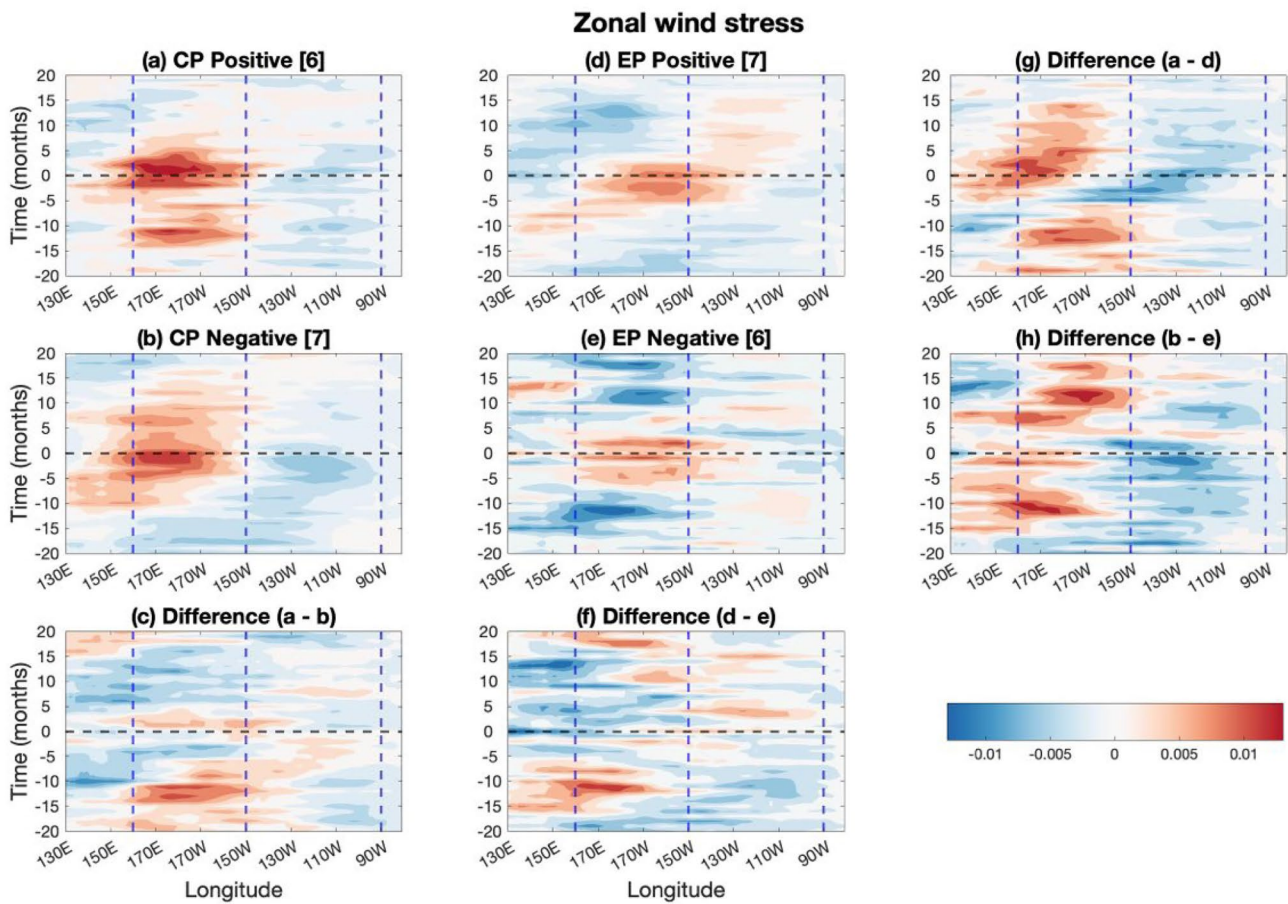
Fig. 10 Composite Hovmöller plots of normalised zonal wind stress anomaly **a** *CP* positive events [6], **b** *CP* negative events [7], **c** difference of positive and negative events of *CP*, **d** *EP* positive events [7], **e** *EP* negative events [6], **f** difference of positive and negative events of *EP*, **g** difference (**a**–**d**), and **h** difference (**b**–**e**). Zonal wind stress anomaly for *CP* positive have been normalised by *CP* index for mean positive events and *EP* positive have been normalised by *EP* index for mean positive events, and similar for negative events. The dashed vertical lines mark the zonal boundaries of the NINO4 (left to centre) and NINO3 (centre to right) regions

of SST does not force *h* as much as the *T* or *EP* related SST patterns. To test this hypothesis, we will be using McGregor et al. (2007), Neske and McGregor (2018) and Neske et al. (2021) approach of forcing the SWM thermocline depth with different spatial wind stress patterns related to the *EP* and *CP* SST pattern to analyse the instantaneous and adjusted thermocline depth response. While the instantaneous thermocline depth response is important feedback to amplify the SST variability, it is the adjusted thermocline depth response that is driving the phase transitions of the ENSO phase space.

Figure 12 shows results of the SWM forced with observed (ERA) wind stress. If the SWM is forced with the entire wind stress field from the ERA data, the mean thermocline depth has a correlation with *h* of about 0.61. The moderate correlation indicates that the SWM could potentially benefit from including higher order baroclinic modes and possibly more realistic western and eastern boundaries (i.e., linear continuously stratified model utilised in Izumo et al. 2019).

The thermocline depth resulting from the SWM simulations forced with wind stress related to the *CP* and *EP* index (Fig. 1a, b) does show some interesting characteristics (Fig. 12). We can first of all notice that the thermocline depth variations related to the *CP* index are smaller than those of the *EP* index. More interestingly they have a very different relation to the SST (Fig. 12b). For the *CP* index we find a mostly in-phase positive correlation, suggesting that most of the forced thermocline depth response is an instantaneous response. Whereas, for the *EP* index we find mostly negative correlations and a clear out-of-phase correlation when the SST leads thermocline depth, consistent with a strong adjusted thermocline depth response. This suggest that the *EP* related wind stress can force a significant phase transition in the ENSO cycle, whereas the *CP* related wind stress do not as clearly.
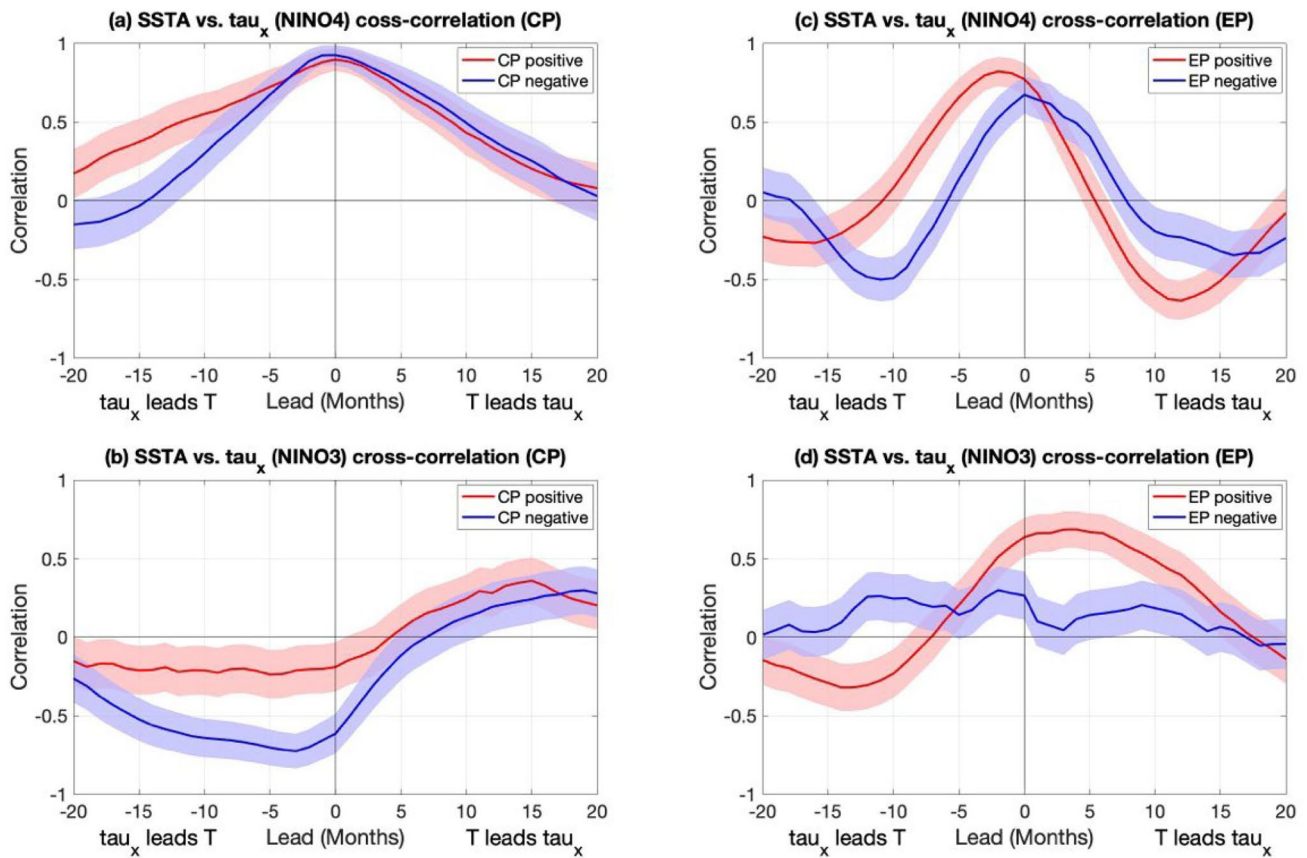
Fig. 11 Cross-Correlation of SSTA for *EP* and *CP* vs. tau$_x$ for positive (red) and negative (blue) events with associated standard error (shaded area) for **a** *CP* for NINO4 region, **b** *CP* for NINO3 region, **c** *EP* for NINO4 region, **d** *EP* for NINO3 region

5.4 Transitions between EP and CP

So far, we presented ENSO by a 2-dimensional phase space of either *T*, *CP* or *EP* indices, assuming that the *CP* and *EP* indices present independent phase spaces. However, it has to be considered that ENSO may not be a 2-dimensional dynamical system, but that there is an interaction between the two indices. We therefore now focus on the analysis of potential interaction between the *CP* and *EP* indices.

Figure 13 shows Hovmöller diagram for the SST anomalies along the equatorial Pacific for *CP* and *EP* events. We can clearly note that the *CP* events are peaking in the central Pacific and the *EP* events peak in the eastern Pacific. We can further note some indication of reversed sign *EP* like SST anomalies preceding negative *CP* events (Fig. 13b) and weak reversed sign *CP* like SST anomalies following positive *EP* events (Fig. 13d). Both of these characteristics would be consistent with the same time evolution: an *EP* El Niño event turning into a *CP* La Niña event.

We can quantify a possible transition from *CP* to *EP* events, by presenting a phase space diagram of the phase transition speed between the *EP* and *CP* index, see Fig. 14a.

Two independent indices should have a phase transition speed not significantly different from zero at all phases. For most phases this is the case for the *EP* and *CP* indices, but in Q2, after an *EP* El Niño phase, there are positive (clockwise) phase transition speeds that appear to be significantly different from zero. This suggests a *CP* La Niña event developing after an *EP* El Niño event, which is also visible in Fig. 13d. The weakly positive phase transition in Q1 suggest that *EP* El Niño event are preceded by a weak *CP* El Niño, which is also weakly present at 10mon to 15mon lead before the positive *EP* events in Fig. 13d.

An alternative transition between *CP* to *EP* events could be via the thermocline depth. The phase space analysis of Figs. 3 and 4 may indicate that the discharge state, which is strong for both indices, maybe a transition from *EP* El Niño events to *CP* La Niña events. To evaluate such a transition, we selected a number of strong discharge states, see Fig. 3 for a phase space presentation of these states. The time evolution of the *EP* and *CP* indices relative to the peak time these discharge states are shown in Fig. 14b.

Here we can note, that before the strong discharge states there are clear positive SST indices, in particular for the
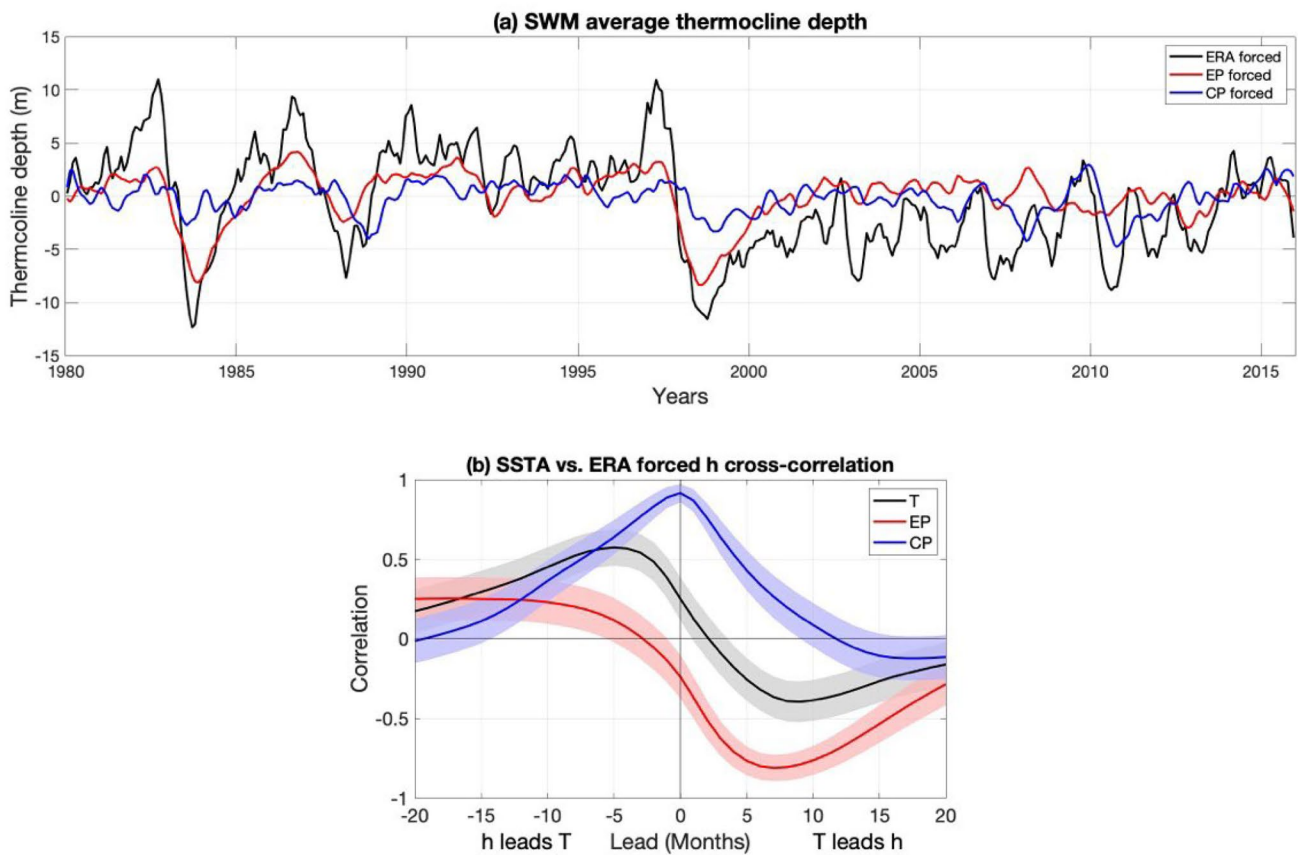
Fig. 12: a Time series of the shallow water model (SWM) thermocline depth for ERA-Interim forced (black), **EP** forced (red) and **CP** forced (blue), **b** cross-correlation between SSTA for **T** vs. **h** from SWM ERA forced (black), **EP** vs. **h** from SWM **EP** forced (red), and SSTA for **CP** vs. **h** from SWM **CP** forced (blue) with associated standard error (shaded area). This thermocline depth used here is eq. pacific **h** for SWM ERA forced.

T and **EP** index. This suggests that strong discharge states mostly follow from **T** and **EP** like El Niño events and less so from **CP** El Niño events. However, after the strong discharge states all three different SST indices are about equally close to zero with a weak negative tendency, not suggesting any preferred type of La Niña events would follow the strong discharge states.

6 Summary and discussions

In this study we investigated the dynamics of **EP** and **CP** type of ENSO variability in the framework of the ReOsc model. We first analysed the phase space characteristics of **EP** and **CP** variability and compared it against the canonical **T** index variability, which is the standard index used to describe the ReOsc model of ENSO. For a better understanding of the differences in the dynamics we further fitted the observed data to linear ReOsc models of the three different pairs of ENSO variability (**T-h**, **CP-h** and **EP-h**), allowing us to determine growth rates, coupling parameters and noise

forcing strength for the different ENSO types. We further supported the analysis by analysing the interaction between equatorial thermocline depth and zonal wind stress. This analysis was further supported by SWM model simulations that allowed us to investigate how the different ENSO pattern of **EP** and **CP** type affect the wind-thermocline forcing.

The results suggest clear dynamical differences between the three indices. Starting with the canonical **T** index, we find that this index describes the oscillating dynamics of ENSO the best, which is consistent with the findings of previous studies (Dommenget and Al-Ansari 2012; Dommenget et al. 2023). It has the ENSO phase space that is closest to the idealised ReOsc model, with the most consistent propagation through all ENSO phases. The coupling between SST and **h** is strongest for this index, leading to the most predictable phase transitions of the different ENSO types.

The **EP** type of ENSO variability is similar to the canonical **T** index, but the ENSO phase space propagations are less clear. It therefore has a less pronounced periodicity that is also slightly shifted to longer time scales. The **EP** type is more asymmetric with clear El Niño extremes, but no
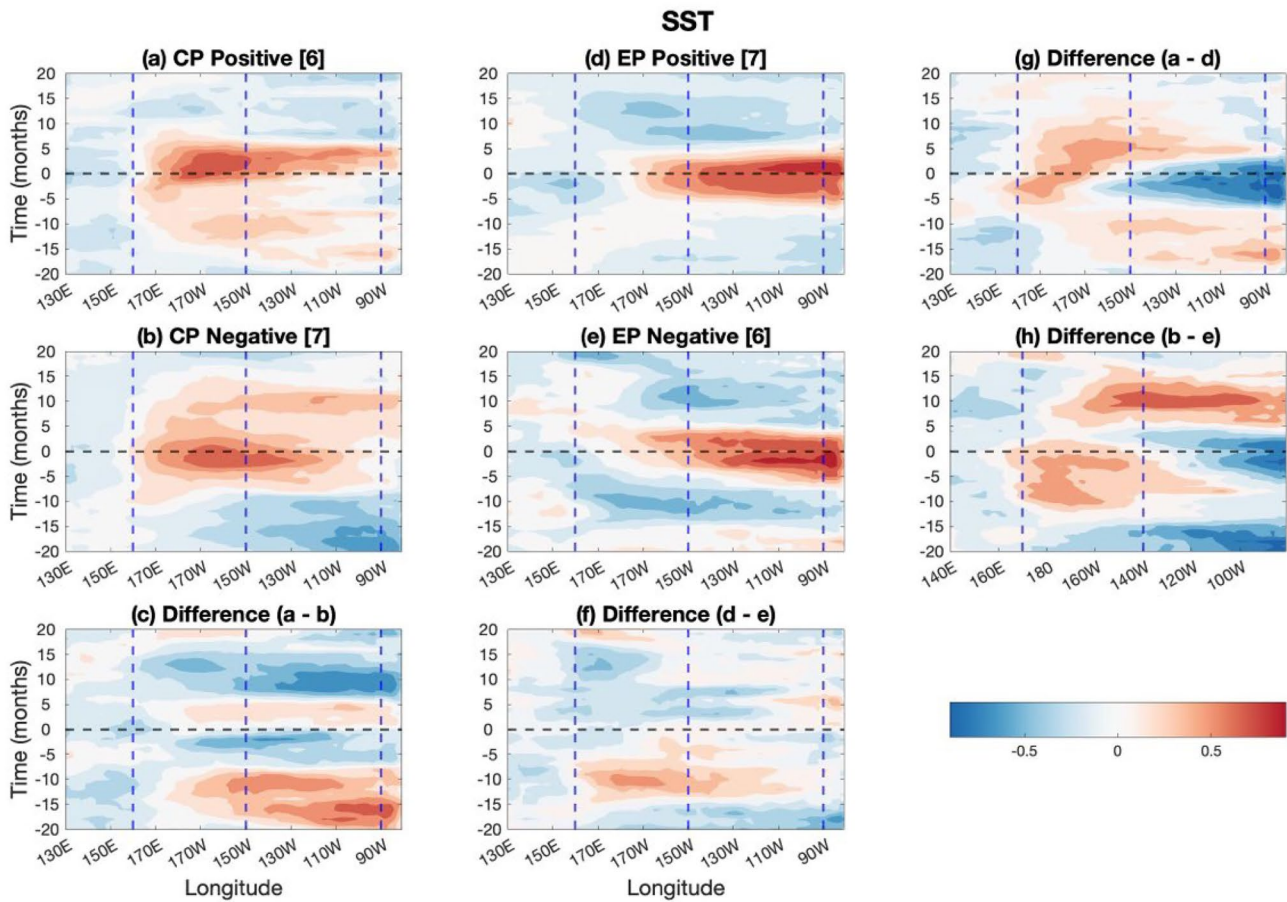
Fig. 13 Composite Hovmöller plots of the normalised SSTA **a** *CP* positive events [6], **b** *CP* negative events [7], **c** difference of positive and negative events of *CP*, **d** *EP* positive events [7], **e** *EP* negative events [6], **f** difference of positive and negative events of *EP*, **g** difference (**a–d**), and **h** difference (**b–e**). SST anomaly for *CP* positive have been normalised by *CP* index for mean positive events and *EP* positive have been normalised by *EP* index for mean positive events, and similar for negative events. The dashed vertical lines mark the zonal boundaries of the NINO4 (left to centre) and NINO3 (centre to right) regions

strong La Niña events, which is consistent with the previous studies (Takahashi et al. 2011; Dommenget et al. 2013). The linear ReOsc model fit suggest a stronger damping of the thermocline, which is further leading to an asymmetric interaction between SST and h, where the SST is less forced by h, but h is clearly forced by SST. Thus, *EP* type El Niños are more wind driven than canonical *T* events, but have stronger transition to the discharge state due to the strong SST-h interaction also suggested by previous studies (Xie and Jin 2018; Kirtman 2019; Okumura 2019). However, the transition of the discharge state to La Niña is not as clear as for the canonical *T* index.

The *CP* type of ENSO variability is quite different from the *EP* and the canonical *T* type. The phase space transitions are fairly weak and chaotic, suggesting it does not have clear interactions between SST and h. This is also supported by the ReOsc model fit, which suggests that the coupling between SST and h is much weaker than in the canonical *T* type, consistent with the findings by Kao

and Yu (2009). The analysis suggests the time scales are shifted to longer time-scales with much less of a clear peak periodicity. This suggest the *CP* type of ENSO is more like red noise with no clear interannual oscillation. This is further supported by SWM simulations that suggest that *CP* type wind forcing does not significantly affect the thermocline tendencies leading to no substantial delayed thermocline anomalies that could provide a phase change of the ENSO mode.

The *CP* type of ENSO variability is also strongly skewed to La Niña extremes, suggesting it mostly describes strong La Niña events, which agrees with the previous studies by Takahashi et al. (2011) and Dommenget et al. (2013). Combined with the above findings, this suggest the La Niña events are more long lasting with less of a clear termination by thermocline anomalies or transitions to recharge states. The phase dependent growth rate suggested that the *CP* events are collapsing after the La Niña state, leading to no clear transition to recharge states.
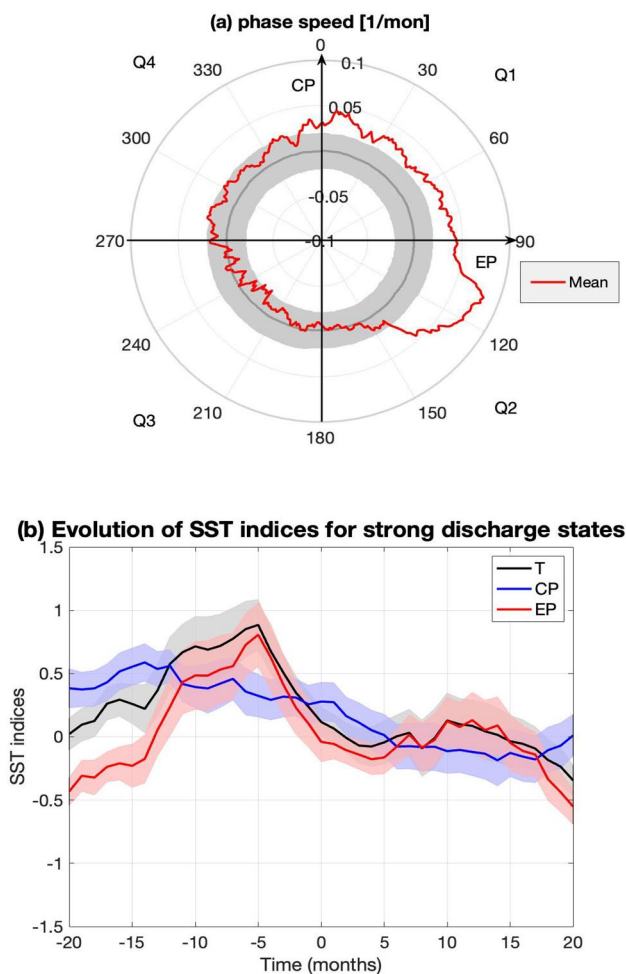
Fig. 14 a Statistics of the observed mean phase speed (red) for *EP* vs. *CP* with uncoupled ReOsc model (grey line) and standard error (shaded area), **b** Time series for the evolution of SST indices: *T* index (black), *CP* index (blue), and *EP* index (red) for strong discharge state (solid line) with associated standard error (shaded area)

The linear ReOsc model can explain some of the important differences between the different ENSO types, but it does not capture the major asymmetry between El Niño and La Niña extremes in the three different ENSO types. Similarly, simple non-linear models considering a non-linear growth rate (a_{11}) also do not capture the phase space characteristics that well (e.g., Dommenget and Al-Ansari 2012 or Dommenget et al. 2023). It requires further analysis to address what non-linear process could explain the non-linear behaviour in the ENSO phase space seen in all three ENSO types.

The idea that *EP* and *CP* type are independent modes of variability is an idealisation, that has limited applications and only reflect some important elements of the ENSO continuum. Although we followed this idea implicitly in our approach, we also tested for possible interactions between the statistical modes. We found some weak interaction that

suggest that *EP* El Niño events tend to transition towards weak *CP* La Niña events. We also found an even weaker indication that *CP* El Niño events can transition weakly into *EP* El Niño events, which could be viewed as the eastward propagation of SSTA. We found no indication for other transitions between the two indices, and also found no indication of transitions between the two types via discharge states, that appear strong for both types of ENSO variability.

Declarations

References

An SI, Jin FF (2004) Nonlinearity and asymmetry of ENSO. J Clim 17(12):2399–2412. https://doi.org/10.1175/1520-0442(2004) 017%3C2399:NAAOE%3E2.0.CO;2

Ashok K, Behera SK, Rao SA, Weng H, Yamagata T (2007) El Niño Modoki and its possible teleconnection. J Geophys Res Oceans. https://doi.org/10.1029/2006JC003798

Bellenger H, Guilyardi É, Leloup J, Lengaigne M, Vialard J (2014) ENSO representation in climate models: from CMIP3 to CMIP5. Clim Dyn 42(7):1999–2018. https://doi.org/10.1007/s00382-013-1783-z

Bjerknes J (1969) Atmospheric teleconnections from the equatorial Pacific. Mon Weather Rev 97(3):163–172. https://doi.org/10.1175/1520-0493(1969)097%3C0163:ATFTEP%3E2.3.CO;2

Burgers G, Jin FF, Van Oldenborgh GJ (2005) The simplest ENSO recharge oscillator. Geophys Res Lett. https://doi.org/10.1029/2005GL022951

Capotondi A, Ricciardulli L (2021) The influence of pacific winds on ENSO diversity. Sci Rep 11(1):1–11. https://doi.org/10.1038/s41598-021-97963-4

Capotondi A, Wittenberg AT, Newman M, Di Lorenzo E, Yu JY, Braconnot P, Yeh SW (2015) Understanding ENSO diversity. Bull Am Meteorol Soc 96(6):921–938. https://doi.org/10.1175/BAMS-D-13-00117.1

Capotondi A, Wittenberg AT, Kug JS, Takahashi K, McPhaden MJ (2020) ENSO diversity. El Niño Southern Oscillation in a Changing Climate. https://doi.org/10.1002/9781119548164.ch4

Carton JA, Giese BS (2008) A reanalysis of ocean climate using simple ocean data assimilation (SODA). Mon Weather Rev 136(8):2999–3017. https://doi.org/10.1175/2007MWR1978.1

Chen M, Li T (2021) ENSO evolution asymmetry: EP versus CP El Niño. Clim Dyn 56(11):3569–3579. https://doi.org/10.1007/s00382-021-05654-7

Choi KY, Vecchi GA, Wittenberg AT (2013) ENSO transition, duration, and amplitude asymmetries: role of the nonlinear wind stress coupling in a conceptual model. J Clim 26(23):9462–9476. https://doi.org/10.1175/JCLI-D-13-00045.1

Crespo LR, Rodríguez-Fonseca MB, Polo I, Keenlyside N, Dommenget D (2022) Multidecadal variability of ENSO in a recharge oscillator framework. Environ Res Lett 17(7):074008. https://doi.org/10.1088/1748-9326/ac72a3

Dee DP, Uppala S (2009) Variational bias correction of satellite radiance data in the ERA-Interim reanalysis. Quart J R Meteorol Soc A J Atmos Sci Appl Meteorol Phys Oceanogr 135(644):1830–1841. https://doi.org/10.1002/qj.493

Dommenget D, Al-Ansari M (2022) Asymmetries in the ENSO phase space. Clim Dyn. https://doi.org/10.1007/s00382-022-06392-0

Dommenget D, Vijayeta A (2019) Simulated future changes in ENSO dynamics in the framework of the linear recharge oscillator model. Clim Dyn 53(7):4233–4248. https://doi.org/10.1007/s00382-019-04780-7

Dommenget D, Bayr T, Frauen C (2013) Analysis of the non-linearity in the pattern and time evolution of El Niño southern oscillation. Clim Dyn 40(11):2825–2847. https://doi.org/10.1007/s00382-012-1475-0

Dommenget D, Priya P, Vijayeta A (2023) ENSO phase space dynamics with an improved estimate of the thermocline depth. Clim Dyn. https://doi.org/10.1007/s00382-023-06883-8

Frauen C, Dommenget D (2010) El Niño and La iña amplitude asymmetry caused by atmospheric feedbacks. Geophys Res Lett. https://doi.org/10.1029/2010GL044444

Good SA, Martin MJ, Rayner NA (2013) EN4: quality controlled ocean temperature and salinity profiles and monthly objective analyses with uncertainty estimates. J Geophys Res Oceans 118(12):6704–6716. https://doi.org/10.1002/2013JC009067

Hasselmann K (1976) Stochastic climate models part I. Theory Tellus 28(6):473–485. https://doi.org/10.1111/j.2153-3490.1976.tb00696.x

Hersbach H, Bell B, Berrisford P, Hirahara S, Horányi A, Muñoz-Sabater J, Thépaut JN (2020) The ERA5 global reanalysis. Quart J R Meteorol Soc 146(730):1999–2049. https://doi.org/10.1002/qj.3803

Izumo T, Vialard J, Dayan H, Lengaigne M, Suresh I (2016) A simple estimation of equatorial Pacific response from windstress to untangle Indian Ocean Dipole and Basin influences on El Niño. Clim Dyn 46:2247–2268. https://doi.org/10.1007/s00382-015-2700-4

Izumo T, Lengaigne M, Vialard J, Suresh I, Planton Y (2019) On the physical interpretation of the lead relation between warm water volume and the El Niño Southern Oscillation. Clim Dyn 52:2923–2942. https://doi.org/10.1007/s00382-018-4313-1

Jansen MF, Dommenget D, Keenlyside N (2009) Tropical atmosphere–ocean interactions in a conceptual framework. J Clim 22(3):550–567. https://doi.org/10.1175/2008JCLI2243.1

Jeong HI, Ahn JB (2017) A new method to classify ENSO events into eastern and central Pacific types. Int J Climatol 37(4):2193–2199. https://doi.org/10.1002/joc.4813

Jin FF (1997) An equatorial ocean recharge paradigm for ENSO. Part I: conceptual model. J Atmos Sci 54(7):811–829. https://doi.org/10.1175/1520-0469(1997)054%3C0811:AEORPF%3E2.0.CO;2

Jin FF, An SI (1999) Thermocline and zonal advective feedbacks within the equatorial ocean recharge oscillator model for ENSO. Geophys Res Lett 26(19):2989–2992. https://doi.org/10.1029/1999GL002297

Kao HY, Yu JY (2009) Contrasting eastern-Pacific and central-Pacific types of ENSO. J Clim 22(3):615–632. https://doi.org/10.1175/2008JCLI2309.1

Kessler WS (2002) Is ENSO a cycle or a series of events? Geophys Res Lett 29(23):40–41. https://doi.org/10.1029/2002GL015924

Kirtman B (2019) ENSO diversity. Clim Dyn 52(12):7133–7133. https://doi.org/10.1007/s00382-019-04723-2

Kug JS, Jin FF, An SI (2009) Two types of El Niño events: cold tongue El Niño and warm pool El Niño. J Clim 22(6):1499–1515. https://doi.org/10.1175/2008JCLI2624.1

Kug JS, Choi J, An SI, Jin FF, Wittenberg AT (2010) Warm pool and cold tongue El Niño events as simulated by the GFDL 2.1 coupled GCM. J Clim 23(5):1226–1239. https://doi.org/10.1175/2009JCLI3293.1

McGregor S, Holbrook NJ, Power SB (2007) Interdecadal sea surface temperature variability in the equatorial Pacific Ocean Part I: the role of off-equatorial wind stresses and oceanic Rossby waves. J Clim 20(11):2643–2658. https://doi.org/10.1175/JCLI4145.1

McPhaden MJ, Zebiak SE, Glantz MH (2006) ENSO as an integrating concept in earth science. Science 314(5806):1740–1745. https://doi.org/10.1126/science.1132588

Meinen CS, McPhaden MJ (2000) Observations of warm water volume changes in the equatorial Pacific and their relationship to El Niño and La Niña. J Clim 13(20):3551–3559. https://doi.org/10.1175/1520-0442(2000)013%3c3551:OOWWVC%3e2.0.CO;2

Neske S, McGregor S (2018) Understanding the warm water volume precursor of ENSO events and its interdecadal variation. Geophys Res Lett 45(3):1577–1585. https://doi.org/10.1002/2017GL076439

Neske S, McGregor S, Zeller M, Dommenget D (2021) Wind spatial structure triggers ENSO's oceanic warm water volume changes. J Clim 34(6):1985–1999. https://doi.org/10.1175/JCLI-D-20-0040.1

Ohba M, Ueda H (2009) Role of nonlinear atmospheric response to SST on the asymmetric transition process of ENSO. J Clim 22(1):177–192. https://doi.org/10.1175/2008JCLI2334.1

Okumura YM (2019) ENSO diversity from an atmospheric perspective. Curr Clim Change Rep 5(3):245–257. https://doi.org/10.1007/s40641-019-00138-7

Okumura YM, Deser C (2010) Asymmetry in the duration of El Niño and La Niña. J Clim 23(21):5826–5843. https://doi.org/10.1175/2010JCLI3592.1

Philander SG (1989) El Niño, La Niña, and the southern oscillation. Int Geophys Ser 46:X-289

Rayner NAA, Parker DE, Horton EB, Folland CK, Alexander LV, Rowell DP, Kent EC, Kaplan A (2003) Global analyses of sea surface temperature, sea ice, and night marine air temperature since the late nineteenth century. J Geophys Res Atmos. https://doi.org/10.1029/2002JD002670

Rebert JP, Donguy JR, Eldin G, Wyrtki K (1985) Relations between sea level, thermocline depth, heat content, and dynamic height in the tropical Pacific Ocean. J Geophys Res Oceans 90(C6):11719–11725. https://doi.org/10.1029/JC090iC06p11719

Takahashi K, Montecinos A, Goubanova K, Dewitte B (2011) ENSO regimes: reinterpreting the canonical and Modoki El Niño. Geophys Res Lett. https://doi.org/10.1029/2011GL047364

Timmermann A, An SI, Kug JS, Jin FF, Cai W, Capotondi A, Zhang X (2018) El Niño–southern oscillation complexity. Nature 559(7715):535–545. https://doi.org/10.1038/s41586-018-0252-6

Tudhope AW, Chilcott CP, McCulloch MT, Cook ER, Chappell J, Ellam RM, Lea DW, Lough JM, Shimmield GB (2001) Variability in the El Niño-southern oscillation through a glacial-interglacial cycle. Science 291(5508):1511–1517. https://doi.org/10.1126/science.1057969

Vijayeta A, Dommenget D (2018) An evaluation of ENSO dynamics in CMIP simulations in the framework of the recharge oscillator model. Clim Dyn 51(5):1753–1771. https://doi.org/10.1007/s00382-017-3981-6

Wang C, Picaut J (2004) Understanding ENSO physics—a review. Earth's Clim Ocean Atmos Interact Geophys Monogr 147:21–48

Webster PJ, Magana VO, Palmer TN, Shukla J, Tomas RA, Yanai MU, Yasunari T (1998) Monsoons: processes, predictability, and the prospects for prediction. J Geophys Res Oceans 103(C7):14451–14510. https://doi.org/10.1029/97JC02719

Wengel C, Dommenget D, Latif M, Bayr T, Vijayeta A (2018) What controls ENSO-amplitude diversity in climate models? Geophys Res Lett 45(4):1989–1996. https://doi.org/10.1002/2017GL076849

Wolter K, Timlin MS (2011) El Niño/Southern Oscillation behaviour since 1871 as diagnosed in an extended multivariate ENSO index (MEI ext). Int J Climatol 31(7):1074–1087. https://doi.org/10.1002/joc.2336

Xie R, Jin FF (2018) Two leading ENSO modes and El Niño types in the Zebiak-Cane model. J Clim 31(5):1943–1962. https://doi.org/10.1175/JCLI-D-17-0469.1

Yang C, Masina S, Storto A (2017) Historical ocean reanalyses (1900–2010) using different data assimilation strategies. Q J R Meteorol Soc 143(702):479–493. https://doi.org/10.1002/qj.2936

Yeh SW, Cai W, Min SK, McPhaden MJ, Dommenget D, Dewitte B, Collins M, Ashok K, An SI, Yim BY, Kug JS (2018) ENSO atmospheric teleconnections and their response to greenhouse gas forcing. Rev Geophys 56(1):185–206. https://doi.org/10.1002/2017RG000568

Yu Y, Dommenget D, Frauen C, Wang G, Wales S (2016) ENSO dynamics and diversity resulting from the recharge oscillator interacting with the slab ocean. Clim Dyn 46(5):1665–1682. https://doi.org/10.1007/s00382-015-2667-1

Yu JY, Giese BS (2013) ENSO diversity in observations. Us Clivar Variat 11(2), Retrieved from https://escholarship.org/uc/item/5bg211kj#

Zhu J, Kumar A, Huang B (2015) The relationship between thermocline depth and SST anomalies in the eastern equatorial Pacific: Seasonality and decadal variations. Geophys Res Lett 42(11):4507–4515. https://doi.org/10.1002/2015GL064220

Zuo H, Balmaseda MA, Tietsche S, Mogensen K, Mayer M (2019) The ECMWF operational ensemble reanalysis–analysis system for ocean and sea ice: a description of the system and assessment. Ocean Sci 15(3):779–808. https://doi.org/10.5194/os-2018-154